Characterization of enriched lithospheric mantle components in ~2.7 Ga Banded Iron Formations: An example from the Tati Greenstone Belt, Northeastern Botswana

Lasse N. Døssing[a,b,*], Robert Frei[a,b], Henrik Stendal[c], Read B.M. Mapeo[d]

[a] Institute of Geography and Geology, University of Copenhagen, Øster Voldgade 10, DK-1350 Copenhagen K, Denmark
[b] Nordic Center for Earth Evolution (NordCEE), Denmark
[c] Geological Survey of Denmark and Greenland (GEUS), Øster Voldgade 10, DK-1350 Copenhagen K, Denmark
[d] Department of Geology, University of Botswana, Private Bag UB 00704, Gaborone, Botswana

A B S T R A C T

Major and trace element, samarium (Sm)–neodymium (Nd) and lead (Pb) isotopic analyses of individual mesobands of five Banded Iron Formations (BIFs) and associated volcanic and sedimentary rocks from the Neoarchean Tati Greenstone Belt (TGB, Northeastern Botswana) were conducted in order to characterize the source(s) and depositional environment(s). Rare earth element (REE)–yttrium (Y) patterns of individual BIF mesobands show features characteristic of other Archean BIFs with LREE depletion relative to MREE and HREE, positive La/La^*_{PAAS}, Eu/Eu^*_{PAAS}, Y/Ho ratios and no Ce/Ce^*_{PAAS} anomalies. The REY patterns are comparable to modern seawater and together with low concentrations of high-field strength elements these features are indicative of an essentially detritus-free precipitation. Elevated Eu anomalies in the TGB BIFs are a general feature observed in ~ 2.7 Ga BIFs worldwide and possibly result from widespread magmatic activity and associated high-temperature fluid fluxes to the oceans at around this time.

Uranogenic Pb isotope data for the BIFs define correlation lines with slopes corresponding to apparent ages of ~2.7 Ga which brackets the depositional timeframe. Pb isotope data on sulfides and Pb-stepwise leaching (PbSL) data on garnets define a correlation line with an apparent age of 1976 ± 88 Ma. This age is similar to tectono-metamorphic events within the adjacent Limpopo belt. Elevated $^{207}Pb/^{204}Pb$ relative to $^{206}Pb/^{204}Pb$ ratios of BIFs are indicative of a high-μ ($^{238}U/^{204}Pb$) prehistory of their source materials which can best be modeled by a 3.0–3.2 Ga extraction of these sources from an older Archean mantle reservoir.

The TGB BIFs show evidence of two periodically interacting water masses during the deposition. The first is characterized by elevated Sm/Nd ratios and a negative inferred ε_{Nd}(2.7 Ga) value of −2.5 and is associated with high Fe fluxes. The second source, associated with high Si fluxes, is characterized by lower Sm/Nd ratios and a less negative inferred ε_{Nd}(2.7 Ga) value of −0.4. While the association of high Fe concentrations and elevated Sm–Nd in BIF mesobands is characteristic of hydrothermal seawater input, the Sm–Nd isotopic characterization of this source, unlike other Archean BIFs, points to a significantly LREE enriched mantle source. This finding is compatible with the potential existence of a sub-continental lithospheric mantle reservoir beneath the Zimbabwe and Kaapvaal craton. The old (up to ~3.5 Ga) Nd (T_{DM}) model ages, particularly of iron-rich mesobands of the TGB BIFs, support such a scenario. In contrast, Si-rich solutes were likely derived from weathering of mafic continental crust.

Keywords:
BIF
Sm–Nd isotopes
Pb isotopes
Trace elements
Botswana

1. Introduction

Banded Iron Formations (BIFs) are thought to represent marine chemical sedimentary rocks that were abundant in the Archean and early Proterozoic (Alibert and McCulloch, 1993; Derry and Jacobsen, 1990; Frei and Polat, 2007). BIFs provide insight to long-term changes in the Earth's evolution, particularly with respect to the chemical composition and oxidation state of ancient seawater and indirectly also to atmospheric changes on land. The chemistry of seawater partly reflects the mixed input from different sources. BIFs are, therefore, useful tracers for some of the main processes controlling the terrestrial Precambrian atmosphere–hydrosphere–lithosphere system (Bau and Möller,

* Corresponding author at: Institute of Geography and Geology, University of Copenhagen, Øster Voldgade 10, DK-1350 Copenhagen K, Denmark.
E-mail address: lnd@geo.ku.dk (L.N. Døssing).

1993; Derry and Jacobsen, 1990). Periodic shifts between silica- and iron-rich mesobands in BIFs are thought to record a balance between submarine hydrothermally versus continentally derived inputs (Hamade et al., 2003; Morris, 1993). Whether these periodic shifts are primary signatures or secondary replacements are a matter of debate (Chown et al., 2000; Mueller and Mortensen, 2002). Major and trace elemental compositions as well as isotopic signatures of individual mesobands and detailed field observations are needed to determine the origin.

The precipitating mechanism for Archean BIFs remains highly debated. Different models have been proposed to explain the oxidation of Fe^{2+} to the less soluble Fe^{3+} and its subsequent precipitation as ferric oxyhydroxides. These include abiotic photochemical oxidation, inorganic reactions using photosynthetically generated O_2, temperature fluctuations in the ocean photic zone and primitive O_2-producing photosynthetic bacteria (Beukes, 2004; Frei and Polat, 2007; Kappler et al., 2005; Konhauser et al., 2002; Posth et al., 2008).

The objectives of this article are: (1) to present isotopic, major- and trace-element data of BIFs and of associated volcanic and sedimentary rocks from the Neoarchean Tati Greenstone Belt (TGB) in order to evaluate the regional geological framework of the TGB; (2) to elaborate on the origin and nature of source materials of the BIFs and to make inferences about the seawater from which these chemical sediments were precipitated. Geochemical data help to distinguish between the two most likely sources—submarine hydrothermal and continental. The results of this article are important because they provide important constraints regarding the TGB, which is important regarding source region characteristics of the surrounding Zimbabwe craton and the adjacent Limpopo Mobile Belt.

2. Geological setting

Southern Africa is largely composed of the Archean Zimbabwe and Kaapvaal cratons (Fig. 1A and B), which are separated by

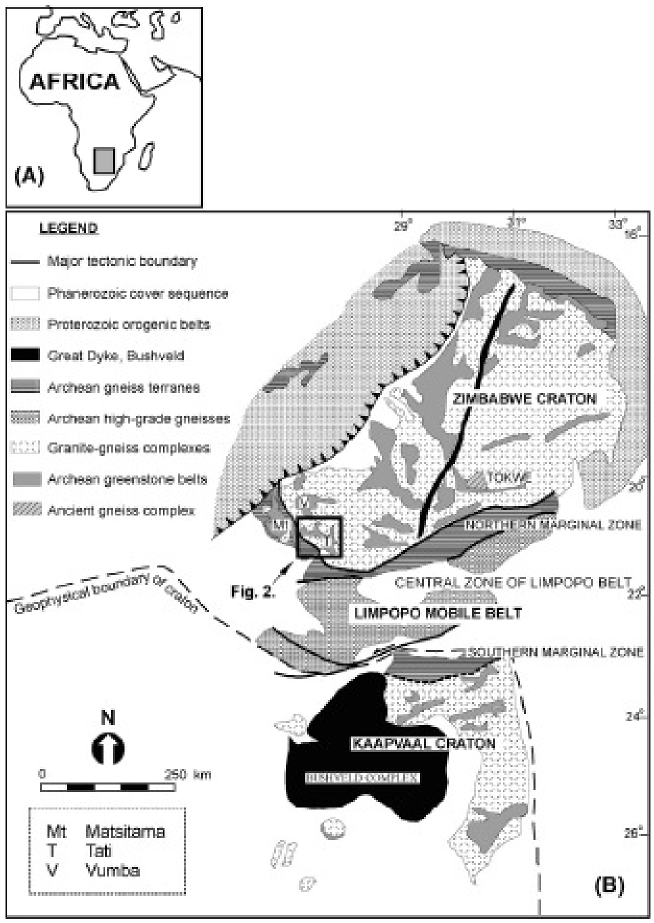

Fig. 1. (A) Sketch map of Africa with inset showing the location of the study area. (B) Simplified geological map of southern Africa; inset depicts the study area enlarged in Fig. 2 (modified after Bagai et al., 2002).

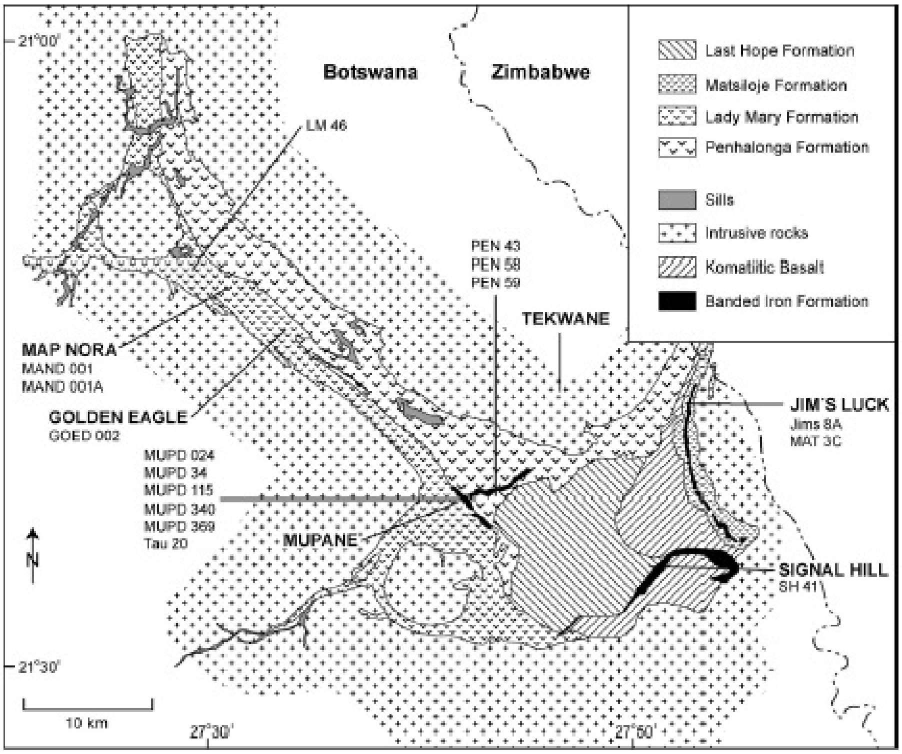

Fig. 2. Simplified geological map of the Tati Greenstone Belt, Northeastern Botswana and adjoining intrusives. Sample locations of BIFs and associated volcanic and sedimentary rocks are indicated and plotted together with the sample number. The study focuses on BIFs from the Mupane, Signal Hill and Jim's Luck areas. Komatiitic Basalt and Banded Iron Formation belong to separate units.

the Limpopo Mobile Belt (LMB). The Zimbabwe craton is composed of several tectono-stratigraphic granite–greenstone terranes emplaced between ~3.5 and ~2.5 Ga and assembled by Neoarchean plate tectonic processes (Wilson et al., 1995). One of these terranes is the central Tokwe crustal segment which consists of ~3.5 Ga gneisses (Dodson et al., 2001; Kusky, 1998). Twenty-three ~2.7 Ga old granite-greenstone belts, including the TGB studied here (Blenkinsop et al., 1997), were subdivided by Kusky (1998) into northern and southern domains flanking the central Tokwe crustal segment. The youngest terrane is composed of ~2.6 Ga granitic plutons that intruded the Tokwe segment and the greenstone belts in a tectonic regime of intracontinental strike–slip faulting, representing a response to the Zimbabwe–Kaapvaal continent–continent collision (e.g. Coward, 1976; Kampunzu et al., 2003; Kusky, 1998).

The Limpopo Mobile Belt defines the southwestern margin of the Zimbabwe craton. It is subdivided into three distinct domains a Northern Marginal Zone, a Central Zone and a Southern Marginal Zone separated by major shear zones (Roering et al., 1992). Zeh et al. (2007) characterized orthogneisses and granitoids from within the Central Zone by zircon U–Pb and Lu–Hf *in situ* laser ablation ICP-MC-MS techniques, which yielded ~2.6–2.7 Ga and 2.02–2.00 Ga age populations. The younger age population is compatible with ~2.02–2.06 PbSL ages, which record tectono-metamorphic events in the Central Zone and Northern Marginal Zone of the Limpopo Mobile Belt (e.g., Berger and Rollinson, 1997; Holzer et al., 1998; Kamber et al., 1995; Kreissig et al., 2000; Kreissig et al., 2001).

Various models have been proposed on the ~2.7 Ga Neoarchean geotectonic evolution and crust stabilization of the Zimbabwe Craton. The continental extensional model suggests that the stabilization of the Zimbabwe Craton was caused by intracratonic rifting related to mantle plume-like magmatism (Bickle et al., 1994; Hunter et al., 1998; Shimizu et al., 2005). Another model suggests emplacement of granite-greenstone terranes and subduction of an oceanic plate under a pre-existing felsic continental crust, possibly represented by the Tokwe segment (Bagai et al., 2002; Kampunzu et al., 2003; Kusky and Kidd, 1992; Zhai et al., 2006). Kusky (1998) suggested that the southern domain of the granite-greenstone belts represents an oceanic suture which closed at ~2.7 Ga. A continental active margin setting for the southwestern part of the proto-Zimbabwe Craton (McCourt et al., 2004) is consistent with shortening and Neoarchean thrusting of the Limpopo Mobile Belt (Coward, 1976; Dirks and Jelsma, 1998). The southwestern margin of the Zimbabwe Craton extends into northeastern Botswana, where the TGB is located (Fig. 2). The inferred total thickness of the TGB is 7–8 km (Fig. 3) which Key (1976) described as a complex succession of mafic to felsic volcanic rocks together with sedimentary rocks, which form a NW-SE trending belt approximately 70 km long and 30 km wide. Key (1976) subdivided the volcanic and sedimentary rocks into three formations on the basis of increasing proportions of felsic volcanic rocks: (1) The Lady Mary Formation

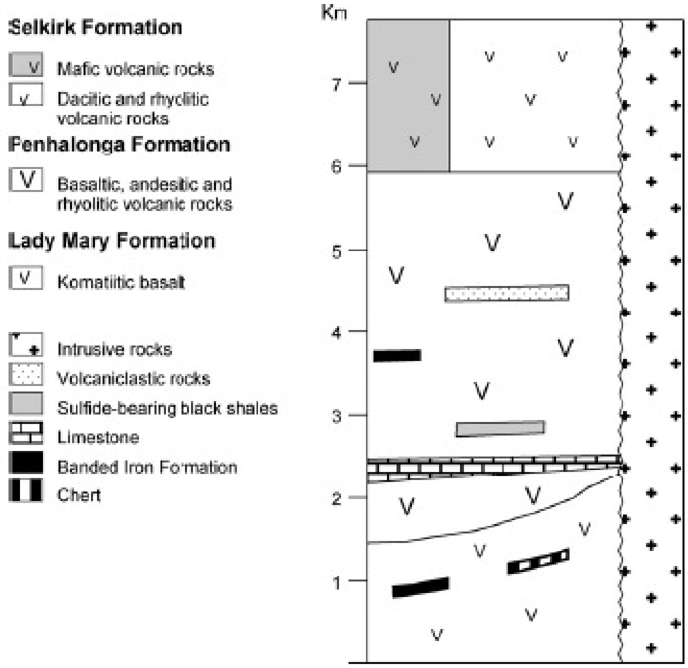

Fig. 3. Generalized stratigraphy of the Tati Greenstone Belt (modified after Key et al., 1976).

constitutes the base of the volcanic and sedimentary rocks and consists of pillow basalt (Fig. 4A and B), altered komatiite and komatiitic basalt and a lesser amount of chert, limestone and BIF. The Lady Mary Formation is host to the Au deposits of Map Nora and Golden Eagle (Fig. 2). (2) The overlying Penhalonga Formation consists of basaltic, andesitic and rhyolitic volcanic rocks, volcaniclastic rocks, limestone, sulfide-bearing black shales and BIFs (Fig. 5A and B). The Penhalonga Formation is host to the Mupane Au deposit which is divided into three open pits: Tau, Kwena and Tholo. (3) Finally, the Selkirk Formation forms the stratigraphically youngest rock sequence. It consists of dacitic and rhyolitic volcanic rocks and less abundant mafic volcanic rocks. The total thickness of the Mupane mine BIFs is approximately 100 m and is well constrained by drill cores. In the Mupane mine the BIFs are in contact with epiclastic sediments rocks such conglomerates, limestones and shales. The total thickness of the Jim's Luck and Signal Hill BIFs is difficult to assess due to poor outcrop but is in the order of tens of meters. The volcanic and sedimentary rocks of the TGB are surrounded and locally intruded by massive granitoids.

There are no accurate published age determinations on the intrusive rocks of the TGB, but granitoid intrusives in the adjacent Vumba greenstone belt (Fig. 1B) yielded zircon U–Pb SHRIMP ages

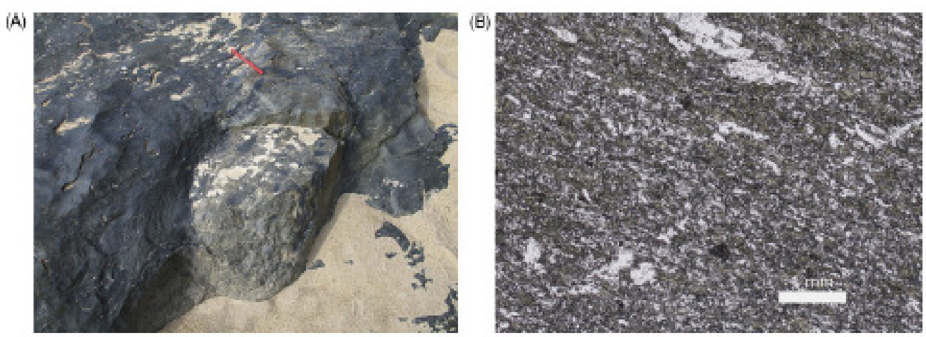

Fig. 4. Photographs of pillow basalt from the Lady Mary Formation. (A) The pillow basalt in outcrop. Pencil is 15 cm. (B) Thin section photograph in plane polarized light of pillow basalt shows fine grained pyroxene, plagioclase and quartz.

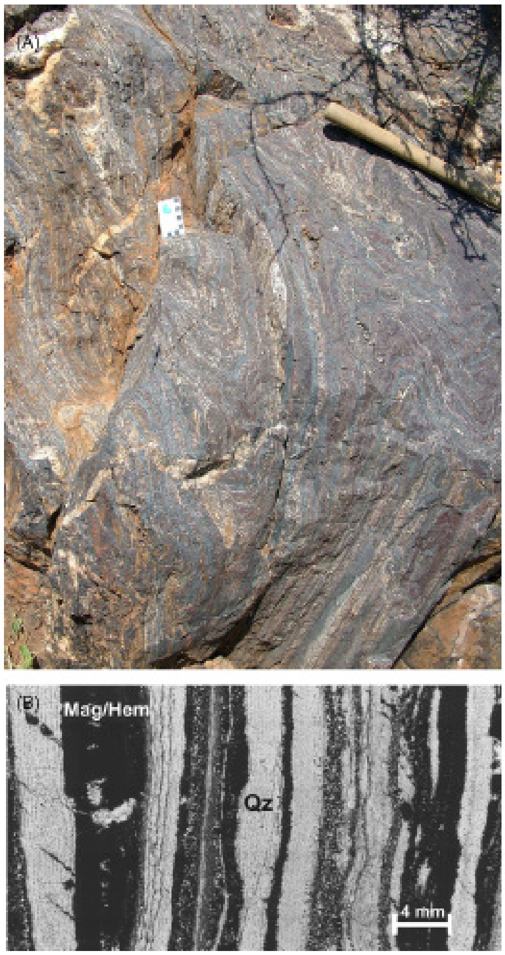

Fig. 5. Photographs of typical oxide facies BIFs from the Tati Greenstone Belt. (A) Outcrop of *in situ*, highly weathered and folded BIF. Scale is 15 cm. (B) Thin section photograph in plane polarized light of BIF shows white bands of crystallized quartz (Qz) and black oxide-facies magnetite/hematite bands (Mag/Hem).

of 2647 ± 4 to 2696 ± 4 Ma (Bagai et al., 2002). The continuation of granitoid bodies between Tati and Vumba greenstone belts suggest similar emplacement ages for the Tati and Vumba intrusives (Key et al., 1976). These ages are supported by granitoid intrusives within the adjacent Matsitama greenstone belt (Fig. 1B), which gave zircon U–Pb SHRIMP ages of 2646 ± 3 to 2710 ± 19 Ma (Majaule and Davis, 1998). The Neoarchean emplacement age of ~2.7 Ga for these intrusives serves as a minimum age constraint for the Vumba and Matsitama greenstone belts and, by inference, for the TGB volcanic and sedimentary successions.

The TGB rocks have been overprinted by lower greenschist to lower amphibolite faces poly-metamorphism and were deformed several times (Key, 1976) resulting in NW–SE striking tectono-stratigraphic units separated by major structural or stratigraphic breaks. Because of poor outcrops, the distribution and stratigraphic correlation between many of the tecono-stratigraphic entities and the geodynamic setting of the TGB are not entirely clear.

3. Sampling and analytical techniques

All of the 63 studied samples were collected during field trips in the spring of 2005 and 2006 to the TGB. Some of the samples are part of drill cores provided by the mining company IAMGold (former Gallery Gold). Additional samples were collected in the open pits of the Mupane mine. The remaining samples were collected from suitable outcrops. BIFs were sampled both in the eastern part of the TGB from Jim's Luck (Jims and MAT) and Signal Hill (SH) and in the Mupane mine pits (MUPD and Tau) (Fig. 2). The volcanic and sedimentary rocks were collected from different locations within the TGB. GPS coordinates for the sample locations are shown in Table 3. Samples include basalts, conglomerates, cherts and garnet-bearing shales. The prefix 'meta' has been omitted to simplify rock description. The sample labeling terminology is as follows: Sample numbers with a hyphen are part of a drill core sample, with the abbreviated labels denoting the drill core location. The number in front of the hyphen defines the drill core number and the number following the hyphen indicates the depth (in meters). For example, GOED 001-36 is a sample from Golden Eagle, from a drill hole labeled 001, taken at 36 m below the surface. Drill cores MUPD 34 and MUPD 115 are from the Tau pit in the Mupane mine (Fig. 2).

The samples were cut with a diamond saw and a representative slice was used to prepare a thin section. BIF specimens were cut into silica- and iron-rich mesobands (<2 cm thick). All samples were crushed in a steel mortar to grain sizes <~3 mm. They were then milled to powders using an automatic agate mortar (Fritsch pulverisette, type 02.102). Garnet and sulfide (arsenopyrite, pyrrhotite and galena) separates were obtained from crushed whole-rock powders using standard magnetic separation and heavy liquid techniques at the Institute of Geography and Geology, University of Copenhagen (IGG). Final mineral separates were hand picked under a binocular microscope.

Major elements and Ge concentrations were determined using a PANalytical MagiX PRO X-ray fluorescence spectrometer (XRF) at IGG. Trace-element concentrations, including REE and Y, were determined using solution ICP-MS (Inductively Coupled Plasma Mass Spectrometer). The samples were dissolved by standard procedures using HNO_3, HCl and HF and analyzed in a Perkin Elmer Elan 6100 DRC quadrupole ICP-MS at the Rock Geochemical Laboratory of the Geological Survey of Denmark and Greenland using the international BHVO-2 standard for calibration. For a comparison of GEUS analytical results on some standards with published values, see Kalsbeek and Frei (2006, Table 1). The isotopic ratios of Sm, Nd and Pb, plus Sm and Nd isotopic dilution concentrations were determined from separately dissolved powder aliquots using a VG Sector 54 IT Thermal Ionization Mass Spectrometer (TIMS) at IGG. Samples used for isotopic analyses were dissolved using the same recipe as those aliquots prepared for the ICP-MS analyses. A $^{150}Nd/^{147}Sm$ spike was added before the samples were dissolved. Samples were separated over chromatographic columns charged with 12 ml AG50W-X 8 (100–200 mesh) cation resin, where REE fractions were collected. REE fractions were further separated over smaller chromatographic columns containing Eichrom's™ LN resin SPS (Part # LN-B25-S). Samarium isotopes were measured in a static multi-collection mode, whereas Nd isotopes were collected in a multi-dynamic routine. The measured Nd isotope ratios were normalized to $^{146}Nd/^{144}Nd = 0.7219$. The mean value of $^{143}Nd/^{144}Nd$ for our JNdi standard is 0.512105 ± 5 (2σ; $n = 15$). Precision for $^{147}Sm/^{144}Nd$ ratios is better than 2% (2σ).

Table 1
Selected major and trace elements of BIFs and associated volcanic rocks from the TGB.

Sample	Locality/area	Formation (Fm.)	Rock type/mesoband	SiO_2[a]	Fe_2O_3[a]	Al_2O_3[a]	Cr[a]	Sc	Y	La	Ce	Pr	Nd	Sm	Eu	Gd	Tb	Dy	Ho	Er	Tm	Yb	Lu
BIFs																							
Jims Ila A	Jim's Luck	Matsiloje Fm.	Oxide BIF/Fe	39.28	59.13	0.76	2.70	15.36	6.03	3.37	6.70	0.82	3.82	0.82	0.60	1.13	0.14	0.81	0.16	0.47	0.07	0.44	0.07
Jims Ila B	Jim's Luck	Matsiloje Fm.	Oxide BIF/Si	56.52	42.32	0.37	2.00	12.82	4.57	1.77	3.08	0.38	1.82	0.40	0.35	0.62	0.08	0.50	0.10	0.30	0.04	0.27	0.05
Jims Ila C	Jim's Luck	Matsiloje Fm.	Oxide BIF/Fe	35.39	62.84	0.54	1.50	16.20	6.20	2.55	4.37	0.51	2.41	0.52	0.44	0.82	0.10	0.68	0.17	0.44	0.06	0.44	0.08
Jims Ila D	Jim's Luck	Matsiloje Fm.	Oxide BIF/Varv	43.44	55.84	0.26	2.50	16.23	4.44	2.50	4.05	0.47	2.22	0.44	0.36	0.63	0.07	0.43	0.09	0.26	0.04	0.26	0.05
Jims Ila E	Jim's Luck	Matsiloje Fm.	Oxide BIF/Varv	49.40	49.66	0.50	2.30	7.75	2.88	1.17	1.90	0.22	1.05	0.21	0.18	0.34	0.04	0.30	0.07	0.19	0.03	0.20	0.04
MAT 3C-A	Matsiloje	Matsiloje Fm.	Oxide BIF/Si	74.83	24.68	0.28	4.50	1.77	1.25	0.77	1.27	0.15	0.65	0.15	0.09	0.19	0.03	0.19	0.04	0.12	0.02	0.10	0.02
MAT 3C-B	Matsiloje	Matsiloje Fm.	Oxide BIF/Fe	55.51	43.91	0.25	4.30	1.28	1.27	0.91	1.61	0.19	0.82	0.16	0.10	0.21	0.03	0.19	0.04	0.13	0.02	0.14	0.02
MAT 3C-C	Matsiloje	Matsiloje Fm.	Oxide BIF/Fe	41.53	57.64	0.45	4.00	8.80	1.30	0.64	1.09	0.13	0.61	0.14	0.09	0.18	0.03	0.20	0.04	0.13	0.02	0.15	0.02
MAT 3C-D	Matsiloje	Matsiloje Fm.	Oxide BIF/Si	64.39	35.15	0.22	4.40	8.68	0.77	0.68	1.07	0.12	0.45	0.09	0.06	0.12	0.02	0.12	0.03	0.08	0.01	0.08	0.01
MAT 3C-E	Matsiloje	Matsiloje Fm.	Oxide BIF/Varv	49.60	49.78	0.28	4.30	8.18	1.07	0.49	0.86	0.11	0.50	0.12	0.09	0.16	0.03	0.17	0.03	0.11	0.02	0.11	0.02
MAT 3C-F	Matsiloje	Matsiloje Fm.	Oxide BIF/Si	76.87	22.36	0.53	4.60	8.00	0.70	0.42	0.71	0.08	0.33	0.07	0.05	0.09	0.02	0.10	0.02	0.07	0.01	0.09	0.01
MAT 3C-G	Matsiloje	Matsiloje Fm.	Oxide BIF/Fe	38.65	60.21	0.46	3.80	8.00	1.09	0.93	1.57	0.18	0.72	0.16	0.10	0.19	0.03	0.19	0.04	0.12	0.02	0.12	0.02
MAT 3C-H	Matsiloje	Matsiloje Fm.	Oxide BIF/Si	76.31	22.52	0.75	4.50	8.00	0.88	0.77	1.33	0.15	0.57	0.11	0.07	0.14	0.02	0.14	0.03	0.10	0.01	0.11	0.02
MAT 3C-K	Matsiloje	Matsiloje Fm.	Oxide BIF/Varv	50.58	48.26	0.64	4.30	8.00	1.73	1.23	2.28	0.27	1.15	0.27	0.16	0.31	0.05	0.32	0.06	0.19	0.03	0.18	0.03
Tau 2D A	Tau Pit	Penhalonga Fm.	Oxide BIF/Si	62.39	33.23	0.02	1.80	23.19	2.98	1.29	2.32	0.27	1.21	0.25	0.19	0.37	0.05	0.34	0.08	0.25	0.04	0.29	0.05
Tau 2D B	Tau Pit	Penhalonga Fm.	Oxide BIF/Si	86.81	10.92	0.26	2.30	18.22	1.25	0.41	0.78	0.09	0.40	0.09	0.10	0.14	0.02	0.13	0.03	0.10	0.01	0.09	0.02
Tau 2D C	Tau Pit	Penhalonga Fm.	Oxide BIF/Fe	51.76	40.66	0.24	1.80	18.21	5.53	1.76	3.19	0.37	1.65	0.37	0.33	0.55	0.08	0.58	0.13	0.44	0.07	0.47	0.08
Tau 2D D	Tau Pit	Penhalonga Fm.	Oxide BIF/Si	67.39	28.72	0.23	1.70	14.68	2.18	0.56	1.04	0.12	0.57	0.14	0.11	0.23	0.03	0.24	0.05	0.17	0.03	0.18	0.03
Tau 2D E	Tau Pit	Penhalonga Fm.	Oxide BIF/Fe	55.23	39.01	0.33	1.70	14.67	4.24	1.22	2.30	0.27	1.25	0.29	0.23	0.44	0.07	0.46	0.12	0.35	0.05	0.37	0.06
Tau 2D F	Tau Pit	Penhalonga Fm.	Oxide BIF/Fe	46.42	46.39	0.33	1.70	17.39	5.97	2.42	4.41	0.51	2.22	0.45	0.41	0.65	0.10	0.70	0.17	0.52	0.08	0.58	0.10
Tau 2D G	Tau Pit	Penhalonga Fm.	Oxide BIF/Si	65.75	29.49	0.18	1.00	16.20	3.68	0.97	1.76	0.21	1.00	0.24	0.23	0.38	0.06	0.42	0.10	0.31	0.05	0.32	0.05
MUPD 024-58 A	Tholo Pit	Penhalonga Fm.	Oxide BIF/Si	92.62	6.94	0.12	1.90	8.61	0.46	0.22	0.38	0.05	0.23	0.06	0.03	0.07	0.01	0.06	0.01	0.04	0.01	0.03	0.01
MUPD 024-58 B	Tholo Pit	Penhalonga Fm.	Oxide BIF/Fe	67.88	30.87	0.20	1.80	14.42	1.89	1.22	1.91	0.21	0.85	0.20	0.12	0.30	0.04	0.31	0.07	0.22	0.04	0.27	0.05
MUPD 024-58 C	Tholo Pit	Penhalonga Fm.	Oxide BIF/Si	92.43	6.93	0.17	2.60	8.89	0.54	0.30	0.43	0.05	0.22	0.06	0.04	0.08	0.01	0.07	0.02	0.05	0.01	0.05	0.01
MUPD 024-58 D	Tholo Pit	Penhalonga Fm.	Oxide BIF/Fe	56.84	42.18	0.16	2.00	7.51	3.83	0.58	1.41	0.16	0.68	0.21	0.14	0.37	0.06	0.42	0.10	0.33	0.06	0.39	0.07
SH41 A	Signal Hill	Unknown stratigraphic position	Oxide BIF/Varv	48.20	49.93	0.68	2.60	8.65	9.53	5.51	11.79	1.42	6.04	1.35	0.54	1.76	0.24	1.50	0.31	0.88	0.12	0.78	0.12
SH41 B	Signal Hill	Unknown stratigraphic position	Oxide BIF/Fe	29.71	69.33	0.38	4.20	8.52	5.50	3.38	5.77	0.81	3.61	0.77	0.34	0.97	0.13	0.81	0.17	0.49	0.07	0.44	0.07
SH41 C	Signal Hill	Unknown stratigraphic position	Oxide BIF/Si	55.36	44.10	0.30	3.40	19.46	5.08	2.47	4.50	0.60	2.70	0.60	0.28	0.84	0.11	0.69	0.15	0.43	0.06	0.25	0.05
SH41 D	Signal Hill	Unknown stratigraphic position	Oxide BIF/Fe	42.11	57.07	0.39	4.30	16.47	3.81	2.00	3.64	0.49	2.23	0.49	0.23	0.69	0.09	0.54	0.12	0.32	0.04	0.27	0.04
SH41 E	Signal Hill	Unknown stratigraphic position	Oxide BIF/Si	67.88	[illegible]	0.26	2.00	[illegible]	4.20	1.57	3.18	0.90	1.81	0.45	0.22	0.68	0.09	0.56	0.13	[illegible]	0.05	0.32	[illegible]
SH41 F	Signal Hill	Unknown stratigraphic position	Oxide BIF/Fe	26.77	72.17	0.35	4.70	6.22	4.01	3.24	5.43	0.76	3.32	0.65	0.25	0.79	0.10	0.60	0.12	0.35	0.05	0.30	0.04
SH41 G	Signal Hill	Unknown stratigraphic position	Oxide BIF/Si	66.85	31.80	0.93	2.50	7.39	4.59	2.08	6.87	0.53	2.31	0.55	0.25	0.77	0.10	0.67	0.14	0.42	0.06	0.40	0.06
Volcanic rocks																							
LM 46	Lady Mary Farm	Lady Mary Fm.	Basalt	51.99	13.19	14.96	1.50	45.05	16.77	5.38	13.31	1.83	8.45	2.47	0.87	3.26	0.59	3.84	0.81	2.33	0.32	2.10	0.31
MAND 001-67	Map Nora	Lady Mary Fm.	Basalt	45.15	20.71	11.74	1.50	44.60	17.05	4.19	10.80	1.57	7.59	2.33	0.93	3.30	0.62	4.14	0.91	2.66	0.38	2.44	0.37
MAND 001-96.5	Map Nora	Lady Mary Fm.	Basalt	47.56	16.89	11.72	1.60	35.38	12.15	6.31	13.50	1.67	7.06	1.80	0.76	2.44	0.41	2.64	0.55	1.62	0.23	1.55	0.25
MAND 001A-16	Map Nora	Lady Mary Fm.	Basalt	45.36	23.26	11.96	1.20	45.86	21.15	3.73	10.16	1.49	7.93	2.48	0.87	3.68	0.57	3.84	0.80	2.29	0.33	2.15	0.31
GOED 002-45	Golden Eagle	Lady Mary Fm.	Basalt	48.93	8.76	11.71	0.40	38.76	9.87	3.11	6.80	0.88	3.93	1.10	0.51	1.54	0.30	2.02	0.45	1.38	0.21	1.41	0.23
PEX43	Selkirk	Penhalonga Fm.	Basalt	48.99	19.49	12.50	1.50	47.34	19.05	8.24	20.35	2.19	9.25	2.22	0.60	2.92	0.46	3.28	0.71	2.13	0.32	2.10	0.31
MUPD 024-80	Tholo Pit	Penhalonga Fm.	Basalt	53.54	12.30	15.76	1.00	54.09	22.26	6.57	14.03	1.73	7.15	1.83	0.62	2.64	0.51	3.89	1.00	3.38	0.53	3.44	0.45
MUPD 024-183.5	Tholo Pit	Penhalonga Fm.	Basalt	49.47	20.64	13.15	2.30	45.72	14.09	5.09	11.10	1.37	5.83	1.49	0.60	2.08	0.38	2.61	0.58	1.73	0.25	1.66	0.27
MUPD 340-30	Kwena Pit	Penhalonga Fm.	Basalt	53.18	15.49	11.54	0.60	2.58	2.61	0.88	1.67	0.20	0.84	0.21	0.23	0.33	0.05	0.37	0.09	0.27	0.04	0.25	0.04
MUPD 369-356	Tau Pit	Penhalonga Fm.	Basalt	53.52	10.08	13.98	1.80	42.84	14.39	2.02	5.56	0.85	4.37	1.48	0.52	2.18	0.43	2.93	0.65	1.91	0.27	1.73	0.26

Fe = Fe-rich bands; Si = Si-rich bands; Varv = Varved bands.
SiO_2, Fe_2O_3 and Al_2O_3 are in wt%. Remaining elements are in ppm.
[a] Determined by XRF. Remaining elements are determined by ICP-MS.

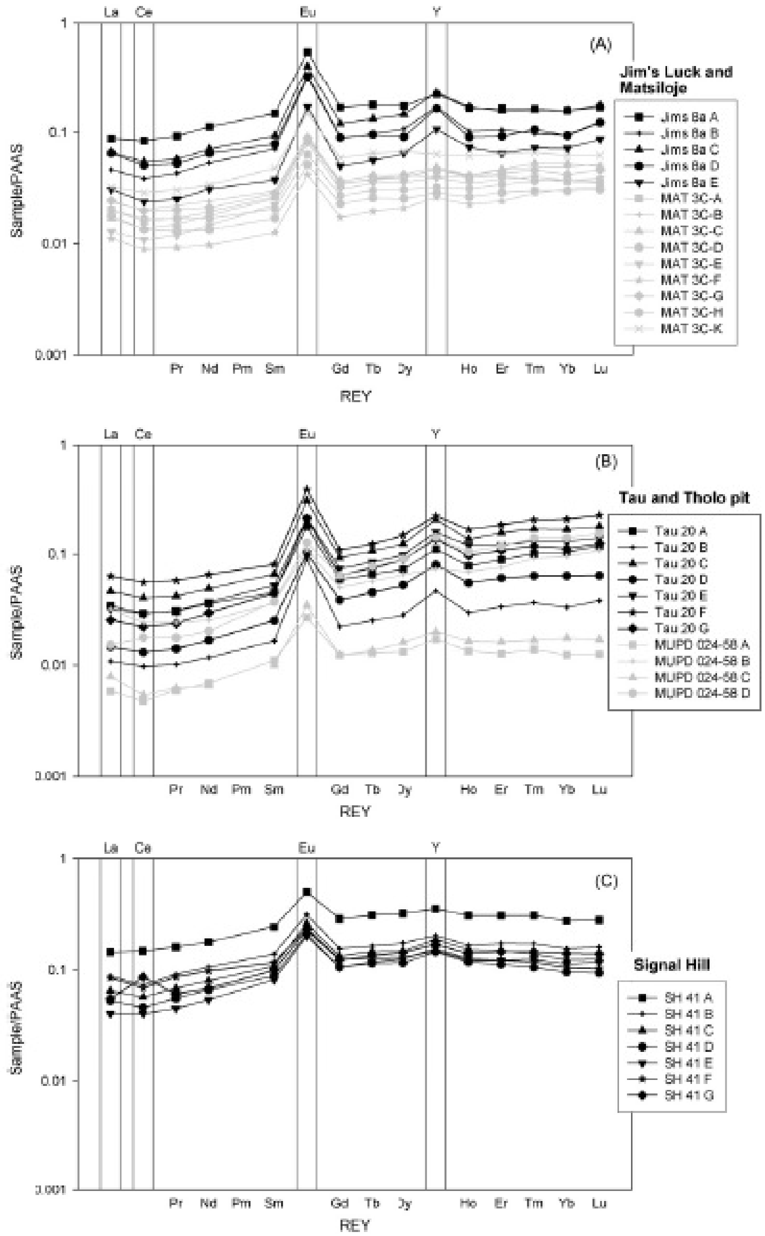

Fig. 6. REY_{PAAS} normalized diagrams of BIFs from the TGB. (A) Oxide-facies BIF from Jim's luck (Matsiloje Formation) and oxide-facies BIF from Matsiloje (Matsiloje Formation); (B) oxide-facies BIF from the Tau pit in the Mupane mine (Penhalonga Formation) and oxide-facies BIF from the Tholo pit in the Mupane mine (Pentalonga Formation); (C) oxide-facies BIF from Signal Hill (unknown stratigraphic position). All of the REY_{PAAS} patterns show LREE and MREE depletion relative to HREE, positive La/La^*_{PAAS}, Eu/Eu^*_{PAAS}, Y/Ho and neither positive ror negative Ce/Ce^*_{PAAS} anomalies. The patterns show typical features of modem seawater with the exception of Ce and Eu anomalies (see text for discussion of the patterns).

Table 2
Quantification of La, Ce, Eu anomalies and selected REY ratios from the TGB BIFs.

Sample	CI Chondrite normalized			PAAS normalized											
	La/La*	Ce/Ce*	Eu/Eu*	La/La*	Ce/Ce*	Eu/Eu*	Eu/Eu**	Y/Ho	$(La/Sm)_{Chon}$	$(Sm/Yb)_{Chon}$	$(Pr/Yb)_{Chon}$	$(Pr/Sm)_{Chon}$	$(Sm/Yb)_{PAAS}$	$(Pr/Yb)_{PAAS}$	$(Pr/Sm)_{PAAS}$
Jimu Ile A	1.34	1.12	2.13	1.67	1.16	3.48	2.45	36.7	2.56	2.06	3.37	1.64	0.95	0.59	0.63
Jimu Ile B	1.58	1.13	2.48	2.11	1.19	3.99	2.81	45.1	2.80	1.64	2.60	1.59	0.75	0.46	0.60
Jimu Ile C	1.64	1.17	2.39	2.07	1.21	3.82	2.69	36.7	3.08	1.29	2.11	1.64	0.59	0.37	0.62
Jimu Ile D	1.81	1.21	2.40	2.39	1.27	3.93	2.77	49.3	3.58	1.83	3.21	1.76	0.84	0.56	0.67
Jimu Ile E	1.78	1.19	2.44	2.32	1.24	3.88	2.73	39.4	3.51	1.14	1.99	1.75	0.52	0.35	0.67
Average	1.70	1.17	2.43	2.22	1.21	3.82	2.69	41.4	3.11	1.59	2.66	1.67	0.73	0.47	0.64
±1σ	0.10	0.03	0.03	0.14	0.04	0.18	0.13	5.0	0.40	0.34	0.56	0.07	0.16	0.10	0.03
MAT 3C-A	1.54	1.11	1.77	1.67	1.10	2.82	1.99	31.4	3.28	1.57	2.63	1.68	0.72	0.46	0.64
MAT 3C-B	1.33	1.04	1.79	1.35	1.02	2.92	2.05	31.2	3.45	1.31	2.55	1.95	0.60	0.45	0.74
MAT 3C-C	1.55	1.11	1.80	1.83	1.13	2.87	2.02	32.6	2.83	1.06	1.62	1.53	0.49	0.28	0.58
MAT 3C-D	1.54	1.12	1.64	1.43	1.06	2.60	1.83	29.7	4.52	1.23	2.50	2.03	0.57	0.44	0.77
MAT 3C-E	1.55	1.13	1.93	1.98	1.18	3.06	2.15	30.5	2.48	1.30	1.82	1.40	0.60	0.32	0.53
MAT 3C-F	1.38	1.06	1.77	1.32	1.01	2.81	1.98	31.6	3.80	0.89	1.72	1.94	0.41	0.30	0.74
MAT 3C-G	1.43	1.09	1.70	1.37	1.05	2.72	1.91	27.4	3.71	1.47	2.72	1.85	0.67	0.48	0.71
MAT 3C-H	1.34	1.08	1.68	1.23	1.01	2.68	1.89	28.4	4.22	1.17	2.52	2.14	0.54	0.44	0.82
MAT 3C-K	1.34	1.09	1.72	1.40	1.07	2.77	1.95	28.2	2.92	1.66	2.77	1.67	0.76	0.49	0.64
Average	1.44	1.09	1.76	1.51	1.07	2.81	1.98	30.1	3.47	1.30	2.32	1.80	0.60	0.41	0.68
±1σ	0.09	0.03	0.08	0.24	0.05	0.13	0.09	1.7	0.63	0.23	0.43	0.23	0.11	0.08	0.09
Tau 20 A	1.49	1.14	2.14	1.70	1.15	3.42	2.41	38.4	3.26	0.93	1.67	1.78	0.43	0.29	0.68
Tau 20 B	1.39	1.13	2.92	1.53	1.13	4.64	3.27	42.8	2.83	1.09	1.76	1.62	0.50	0.31	0.62
Tau 20 C	1.48	1.15	2.40	1.68	1.16	3.78	2.67	41.0	3.01	0.86	1.42	1.66	0.39	0.25	0.63
Tau 20 D	1.44	1.13	2.07	1.71	1.16	3.22	2.27	40.2	2.51	0.86	1.26	1.46	0.40	0.22	0.56
Tau 20 E	1.44	1.15	2.14	1.73	1.18	3.36	2.37	35.7	2.64	0.87	1.35	1.55	0.40	0.24	0.59
Tau 20 F	1.40	1.12	2.53	1.50	1.11	4.02	2.83	36.1	3.38	0.86	1.60	1.87	0.39	0.28	0.71
Tau 20 G	1.59	1.18	2.46	2.13	1.25	3.85	2.71	38.2	2.49	0.85	1.20	1.41	0.39	0.21	0.54
Average	1.47	1.14	2.38	1.77	1.16	3.76	2.65	38.9	2.87	0.90	1.47	1.62	0.42	0.26	0.62
±1σ	0.07	0.02	0.20	0.23	0.04	0.45	0.32	2.4	0.33	0.08	0.20	0.15	0.04	0.03	0.06
MUFD 034-58 A	1.28	0.94	1.39	1.42	0.95	2.28	1.61	34.9	2.26	1.94	2.74	1.41	0.89	0.48	0.54
MUFD 034-58 B	1.53	1.10	1.64	1.45	1.04	2.60	1.83	28.8	3.84	0.82	1.44	1.77	0.38	0.25	0.67
MUFD 034-58 C	1.49	0.96	1.89	1.43	0.92	3.06	2.15	33.4	3.40	1.25	2.02	1.62	0.57	0.35	0.62
MUFD 034-58 D	1.12	1.18	1.65	1.22	1.17	2.51	1.77	37.0	1.77	0.58	0.72	1.25	0.27	0.13	0.48
Average	1.35	1.04	1.64	1.38	1.02	2.61	1.84	33.5	2.82	1.15	1.73	1.51	0.53	0.30	0.58
±1σ	0.17	0.10	0.18	0.10	0.10	0.28	0.20	3.0	0.83	0.52	0.74	0.20	0.24	0.13	0.08
SH 41 A	1.11	1.06	1.15	1.34	1.03	1.87	1.32	31.1	2.56	1.91	3.32	1.73	0.88	0.58	0.66
SH 41 B	1.29	0.95	1.30	1.45	0.95	2.13	1.50	33.3	2.74	1.94	3.35	1.73	0.89	0.59	0.66
SH 41 C	1.27	0.99	1.33	1.44	1.00	2.15	1.52	33.5	2.57	1.90	3.14	1.65	0.87	0.55	0.63
SH 41 D	1.32	1.01	1.34	1.57	1.03	2.17	1.53	33.4	2.57	2.00	3.29	1.64	0.92	0.58	0.62
SH 41 E	1.23	1.08	1.35	1.45	1.10	2.15	1.51	33.6	2.13	1.56	2.26	1.45	0.72	0.40	0.55
SH 41 F	1.26	0.92	1.18	1.35	0.92	1.95	1.37	33.0	3.13	2.43	4.71	1.93	1.12	0.82	0.74
SH 41 G	1.14	1.65	1.28	1.21	1.63	2.06	1.45	33.0	2.36	1.54	2.46	1.60	0.71	0.43	0.61
Average	1.23	1.09	1.28	1.37	1.10	2.07	1.46	33.0	2.58	1.90	3.22	1.68	0.87	0.56	0.64
±1σ	0.07	0.23	0.07	0.14	0.23	0.11	0.08	0.8	0.29	0.28	0.73	0.14	0.13	0.13	0.05

La* = (3 × Pr − 2 × Nd); Ce* = (2 × Pr − 1 × Nd); Eu* = (2/3 × Sm + 1/3 × Tb)
Eu/Eu** = Eu/Eu* normalized to average Eu/Eu* = 1.42 defined by Hamersley BIF (Alibert and McCulloch, 1993).

Table 2
Pb isotope data for BIFs and associated volcanic and sedimentary rocks from the TGB.

Sample	Locality/area	Formation (Fm.)	Rock type/ mesoband	$^{206}Pb/^{204}Pb$	±2σ[a]	$^{207}Pb/^{204}Pb$	±2σ[a]	$^{208}Pb/^{204}Pb$	±2σ[a]	r_1[b]	r_2[c]	Pb[d]	Th[d]	U[d]	$^{206}Pb/^{204}Pb_{(t)}$	$^{207}Pb/^{204}Pb_{(t)}$	$^{208}Pb/^{204}Pb_{(t)}$	Longitude	Latitude
BIFs																			
Jims 8a A	Jim's Luck	Matsiloje Fm.	Oxide BIF/Fe	14.464	0.006	14.941	0.011	34.477	0.029	0.657	0.831	1.75	0.37	0.06	13.713	14.847	33.211	27°51′65″E	21°25′83″S
Jims 8a B	Jim's Luck	Matsiloje Fm.	Oxide BIF/Si	14.380	0.008	14.984	0.010	34.044	0.028	0.666	0.825	2.53	0.13	0.03	14.121	14.852	33.735	27°51′65″E	21°25′83″S
Jims 8a C	Jim's Luck	Matsiloje Fm.	Oxide BIF/Fe	14.236	0.006	14.909	0.011	33.659	0.029	0.625	0.820	1.20	0.18	0.06	13.248	14.786	33.050	27°51′62″E	21°25′83″S
Jims 8a D	Jim's Luck	Matsiloje Fm.	Oxide BIF/Varv	14.568	0.008	14.957	0.010	34.171	0.028	0.661	0.804	1.26	0.20	0.05	13.801	14.861	33.168	27°51′62″E	21°25′83″S
Jims 8a E	Jim's Luck	Matsiloje Fm.	Oxide BIF/Varv	14.539	0.010	15.005	0.012	34.075	0.030	0.650	0.812	1.51	0.11	0.03	14.170	14.960	33.630	27°51′62″E	21°25′83″S
MAT 3C-A	Matsiloje	Matsiloje Fm.	Oxide BIF/Si	16.002	0.044	15.226	0.043	35.527	0.102	0.882	0.876	0.75	0.05	0.03	15.034	15.104	35.069	27°51′65″E	21°25′45″S
MAT 3C-B	Matsiloje	Matsiloje Fm.	Oxide BIF/Fe	14.825	0.018	15.025	0.020	34.360	0.047	0.674	0.860	1.14	0.09	0.06	13.667	14.881	33.879	27°51′65″E	21°25′45″S
MAT 3C-C	Matsiloje	Matsiloje Fm.	Oxide BIF/Fe	15.404	0.014	15.130	0.015	34.887	0.038	0.625	0.840	1.11	0.06	0.09	13.662	14.913	34.567	27°51′65″E	21°25′45″S
MAT 3C-D	Matsiloje	Matsiloje Fm.	Oxide BIF/Si	15.167	0.017	15.085	0.018	34.569	0.045	0.659	0.844	0.72	0.06	0.05	13.810	14.916	34.116	27°51′65″E	21°25′45″S
MAT 3C-E	Matsiloje	Matsiloje Fm.	Oxide BIF/Varv	15.536	0.013	15.143	0.014	35.002	0.036	0.673	0.845	0.78	0.04	0.06	13.848	14.934	34.701	27°51′65″E	21°25′45″S
MAT 3C-F	Matsiloje	Matsiloje Fm.	Oxide BIF/Si	14.956	0.011	15.044	0.013	34.424	0.033	0.664	0.838	0.55	0.03	0.02	14.027	14.929	34.075	27°51′65″E	21°25′45″S
MAT 3C-G	Matsiloje	Matsiloje Fm.	Oxide BIF/Fe	[illegible]	[illegible]	[illegible]	[illegible]	[illegible]	[illegible]	[illegible]	[illegible]	[illegible]	[illegible]	[illegible]	[illegible]	[illegible]	[illegible]	[illegible]	[illegible]
MAT 3C-H	Matsiloje	Matsiloje Fm.	Oxide BIF/Si	14.794	0.010	15.021	0.012	34.341	0.031	0.655	0.830	0.77	0.05	0.03	14.046	14.928	33.871	27°51′65″E	21°25′45″S
MAT 3C-K	Matsiloje	Matsiloje Fm.	Oxide BIF/Varv	15.393	0.012	15.128	0.013	34.918	0.034	0.690	0.840	1.07	0.07	0.06	14.165	14.875	34.540	27°51′65″E	21°25′45″S
Tau 20 A	Tau Pit	Pentalonga Fm.	Oxide BIF/Si	14.462	0.014	15.021	0.016	33.961	0.041	0.690	0.874	2.02	0.06	0.04	14.094	14.975	33.781	27°43′03″E	21°27′37″S
Tau 20 B	Tau Pit	Pentalonga Fm.	Oxide BIF/Si	14.221	0.008	14.908	0.010	33.858	0.027	0.655	0.825	2.45	0.01	0.01	14.110	14.884	33.831	27°43′03″E	21°27′37″S
Tau 20 C	Tau Pit	Pentalonga Fm.	Oxide BIF/Fe	14.367	0.010	14.966	0.012	33.861	0.030	0.672	0.836	4.12	0.06	0.05	14.144	14.958	33.775	27°43′03″E	21°27′37″S
Tau 20 D	Tau Pit	Pentalonga Fm.	Oxide BIF/Si	14.453	0.008	15.015	0.010	34.003	0.027	0.659	0.829	2.58	0.04	0.03	14.396	14.983	33.902	27°43′03″E	21°27′37″S
Tau 20 E	Tau Pit	Pentalonga Fm.	Oxide BIF/Fe	14.568	0.008	15.025	0.010	34.041	0.027	0.659	0.829	2.57	0.08	0.05	14.368	14.975	33.864	27°43′03″E	21°27′37″S
Tau 20 F	Tau Pit	Pentalonga Fm.	Oxide BIF/Fe	14.782	0.008	15.043	0.011	34.228	0.028	0.684	0.833	2.40	0.15	0.09	14.073	14.973	33.913	27°43′03″E	21°27′37″S
Tau 20 G	Tau Pit	Pentalonga Fm.	Oxide BIF/Si	14.309	0.010	15.003	0.012	33.899	0.032	0.670	0.828	3.46	0.04	0.03	14.146	14.983	33.824	27°43′03″E	21°27′37″S
MUPD 024-58 A	Thola Pit	Pentalonga Fm.	Oxide BIF/Si	15.418	0.010	15.263	0.012	34.871	0.031	0.666	0.830	0.60	0.02	0.05	13.662	15.044	34.723	27°43′71″E	21°27′36″S
MUPD 024-58 B	Thola Pit	Pentalonga Fm.	Oxide BIF/Fe	15.495	0.008	15.273	0.011	35.032	0.029	0.662	0.821	2.02	0.10	0.15	13.658	15.082	34.739	27°43′71″E	21°27′36″S
MUPD 024-58 C	Thola Pit	Pentalonga Fm.	Oxide BIF/Si	15.666	0.011	15.294	0.012	35.247	0.032	0.653	0.825	0.50	0.04	0.05	13.415	15.113	34.796	27°43′71″E	21°27′36″S
MUPD 024-58 D	Thola Pit	Pentalonga Fm.	Oxide BIF/Fe	15.766	0.010	15.317	0.011	35.314	0.030	0.690	0.825	1.93	0.65	0.59	9.316	14.513	33.194	27°43′71″E	21°27′36″S
SH 41 A	Signal Hill	Unknown strati-graphic position	Oxide BIF/Varv	17.253	0.010	15.508	0.011	37.199	0.030	0.661	0.833	6.13	0.56	0.28	16.317	15.379	36.597	27°50′79″E	21°28′34″S
SH 41 B	Signal Hill	Unknown strati-graphic position	Oxide BIF/Fe	16.519	0.010	15.353	0.011	36.266	0.031	0.651	0.894	3.50	0.19	0.18	15.425	15.217	35.917	27°50′79″E	21°28′34″S
SH 41 C	Signal Hill	Unknown strati-graphic position	Oxide BIF/Si	16.648	0.013	15.415	0.014	36.403	0.036	0.674	0.830	2.87	0.08	0.17	15.358	15.254	36.222	27°50′79″E	21°28′34″S
SH 41 D	Signal Hill	Unknown strati-graphic position	Oxide BIF/Fe	16.256	0.010	15.319	0.011	35.745	0.030	0.658	0.831	2.13	0.05	0.16	14.639	15.116	35.593	27°50′79″E	21°28′34″S
SH 41 E	Signal Hill	Unknown strati-graphic position	Oxide BIF/Si	16.825	0.010	15.427	0.011	36.319	0.030	0.662	0.836	2.53	0.03	0.17	15.327	15.240	36.233	27°50′79″E	21°28′34″S
SH 41 F	Signal Hill	Unknown strati-graphic position	Oxide BIF/Fe	17.239	0.013	15.474	0.013	36.288	0.035	0.658	0.838	3.07	0.10	0.28	15.240	15.225	36.074	27°50′79″E	21°28′34″S
SH 41 G	Signal Hill	Unknown strati-graphic position	Oxide BIF/Si	16.662	0.011	15.442	0.011	36.587	0.032	0.625	0.820	3.70	0.09	0.18	15.885	15.308	36.427	27°50′79″E	21°28′34″S
Volcanic rocks																			
LM 46	Lady Mary Farm	Lady Mary Fm.	Basalt	20.128	0.011	16.053	0.011	39.728	0.032	0.659	0.809	3.95	1.24	0.29	14.364	14.184	33.956	27°51′80″E	21°18′22″S
MAND 001-67	Map Nora	Lady Mary Fm.	Basalt	15.628	0.008	15.149	0.009	35.630	0.027	0.657	0.833	2.99	0.86	0.26	14.143	14.832	33.827	27°30′20″E	21°19′20″S
MAND 001-96.5	Map Nora	Lady Mary Fm.	Basalt	17.872	0.010	15.505	0.011	37.413	0.030	0.653	0.820	17.27	1.89	0.57	17.121	15.412	36.644	27°30′20″E	21°19′20″S
MAND 001A-16	Map Nora	Lady Mary Fm.	Basalt	18.252	0.011	15.549	0.011	37.691	0.032	0.657	0.817	1.30	0.60	0.18	15.087	15.156	34.569	27°30′20″E	21°19′20″S
GOSTU 002-45	Golden Eagle	Lady Mary Fm.	Basalt	15.318	0.008	15.154	0.010	34.882	0.027	0.658	0.832	8.88	0.81	0.22	14.612	15.061	34.226	27°33′68″E	21°21′30″S
PEN 43	Selkirk	Pentalonga Fm.	Basalt	25.269	0.036	18.820	0.021	54.592	0.064	0.677	0.860	2.00	3.57	0.67	23.761	17.187	36.371	27°47′08″E	21°27′34″S
MUPD 024-80	Thola Pit	Pentalonga Fm.	Basalt	17.068	0.010	15.575	0.011	36.359	0.030	0.648	0.898	1.36	2.27	0.64	6.782	14.394	25.537	27°43′71″E	21°27′36″S
MUPD 024-103.5	Thola Pit	Pentalonga Fm.	Basalt	34.432	0.021	18.040	0.013	53.600	0.046	0.663	0.827	5.74	1.59	0.58	30.652	17.636	53.105	27°43′71″E	21°27′36″S
MUPD 34-238.5	Tau Pit	Pentalonga Fm.	Basalt	14.516	0.006	15.031	0.011	34.190	0.029	0.658	0.828							–	–
MUPD 34-238.5 r	Tau Pit	Pentalonga Fm.	Basalt	14.271	0.004	15.042	0.005	34.045	0.012	0.657	0.838							–	–
MUPD 135-327.5	Tau Pit	Pentalonga Fm.	Basalt	15.525	0.015	15.262	0.017	35.204	0.041	0.670	0.847							–	–
MUPD 340-30	Kwena Pit	Pentalonga Fm.	Basalt	16.566	0.006	15.362	0.010	36.155	0.039	0.659	0.832	2.03	0.05	0.03	16.288	15.328	35.982	27°43′69″E	21°27′36″S
MUPD 369-356	Tau Pit	Pentalonga Fm.	Basalt	14.693	0.009	15.043	0.010	34.374	0.026	0.657	0.832	0.81	0.37	0.11	11.868	14.691	31.589	27°43′73″E	21°27′36″S

Table 3 (Continued)

Sample	Locality/area	Formation (Fm.)	Rock type/ microband	$^{206}Pb/^{204}Pb$	±2σ[a]	$^{207}Pb/^{204}Pb$	±2σ[a]	$^{208}Pb/^{204}Pb$	±2σ[a]	r_1[b]	r_2[c]	Pb[d]	Th[d]	U[d]	$^{206}Pb/^{204}Pb$	$^{207}Pb/^{204}Pb$	$^{208}Pb/^{204}Pb$	Longitude	Latitude
Sedimentary rocks																			
PEN 58	Selkirk	Penhalonga Fm.	Garnet-chert	15.937	0.009	15.080	0.010	35.934	0.029	0.961	0.929	47.9	3.84	0.98	15.169	15.435	33.369	27°47′37″E	21°27′33″S
PEN 59	Selkirk	Penhalonga Fm.	Garnet-chlorite-chert	17.433	0.009	15.559	0.010	37.202	0.029	0.944	0.924	3.50	1.70	0.40	14.878	15.241	33.366	27°47′20″E	21°27′32″S
MUPD 24-238.5	Tau Pit	Penhalonga Fm.	Sulfide-bearing quartz-grunerite-siderite-chert	14.516	0.009	15.031	0.011	34.190	0.029	0.968	0.928							27°43′71″E	21°27′36″S
MUPD 34–158	Tau Pit	Penhalonga Fm.	Chlorite-muscovite-quartz-chert	18.050	0.010	15.551	0.011	36.533	0.030	0.961	0.935							–	–
MUPD 115–185	Tau Pit	Penhalonga Fm.	Sulfide-bearing quartz-grunerite-siderite-chert	14.727	0.007	15.090	0.010	34.329	0.026	0.957	0.932							–	–
MUPD 115–185[e]	Tau Pit	Penhalonga Fm.	Sulfide-bearing quartz-grunerite-siderite-chert	14.524	0.017	15.063	0.018	34.074	0.044	0.979	0.961							–	–
MUPD 115–194	Tau Pit	Penhalonga Fm.	Quartz-grunerite-siderite-BIF	14.172	0.010	15.000	0.012	33.845	0.030	0.957	0.931							–	–
MUPD 115–194 r	Tau Pit	Penhalonga Fm.	Quartz-grunerite-siderite-BIF	14.208	0.017	15.031	0.019	33.958	0.046	0.975	0.960							–	–
MUPD 115–223.5	Tau Pit	Penhalonga Fm.	Garnet-bearing graphite-chert	15.421	0.010	15.348	0.011	35.196	0.033	0.954	0.856							–	–
MUPD 115–237.5	Tau Pit	Penhalonga Fm.	Garnet-chlorite-bearing graphite-chert	14.060	0.016	14.921	0.018	33.779	0.045	0.957	0.910							–	–
MUPD 115–230	Tau Pit	Penhalonga Fm.	Sulfide-bearing graphite chert	[illegible]	[illegible]	[illegible]	[illegible]	[illegible]	[illegible]	[illegible]	[illegible]							–	–
MUPD 115–296 r	Tau Pit	Penhalonga Fm.	Sulfide-bearing graphite chert	13.950	0.004	14.921	0.005	33.707	0.013	0.946	0.869							–	–
MUPD 115–361.5	Tau Pit	Penhalonga Fm.	Garnet-bearing graphite chert	18.035	0.020	15.815	0.018	37.816	0.047	0.974	0.956							–	–

[a] Errors are two standard deviations absolute (Ludwig, 2003).
[b] $r_1 = ^{206}Pb/^{204}Pb$ vs. $^{207}Pb/^{204}Pb$ error correlation (Ludwig, 2003).
[c] $r_2 = ^{206}Pb/^{204}Pb$ vs. $^{208}Pb/^{204}Pb$ error correlation (Ludwig, 2003).
[d] Determined by ICP-MS, values in ppm.
[e] Repeated sample.

Table 4
Pb isotope data of stepwise leach experiments on garnets from sedimentary rocks associated with BIFs in the Tau pit (TGB)

Sample	Locality/area	Formation (Fm.)	Acid	Time	$^{206}Pb/^{204}Pb$	±2σ[a]	$^{207}Pb/^{204}Pb$	±2σ[a]	$^{208}Pb/^{204}Pb$	±2σ[a]	r_1[b]	r_2[c]
MUP0 34-156	Tau Pit	Penhalonga Fm.	Mix	30 min	19.139	0.014	15.708	0.013	38.258	0.036	0.987	0.937
MUP0 34-156	Tau Pit	Penhalonga Fm.	1N HBr	1 h	20.274	0.044	15.848	0.035	38.657	0.087	0.988	0.975
MUP0 34-156	Tau Pit	Penhalonga Fm.	4N HBr	3 h	23.481	0.072	16.124	0.050	41.470	0.130	0.992	0.990
MUP0 34-156	Tau Pit	Penhalonga Fm.	8.8N HBr	6 h	20.491	0.081	15.789	0.063	37.251	0.150	0.992	0.990
MUP0 34-156	Tau Pit	Penhalonga Fm.	8.8N HBr	17 h	18.349	0.060	15.551	0.051	35.881	0.120	0.992	0.987
MUP0 34-156	Tau Pit	Penhalonga Fm.	HF conc.	17 h	24.690	0.048	16.403	0.033	35.891	0.074	0.979	0.971
MUP0 34-156	Tau Pit	Penhalonga Fm.	HF conc.	96 h	22.862	0.266	16.160	0.189	37.208	0.435	0.995	0.987
MUP0 115-223.5	Tau Pit	Penhalonga Fm.	Mix	30 min	18.829	0.016	15.619	0.015	38.629	0.040	0.974	0.949
MUP0 115-223.5	Tau Pit	Penhalonga Fm.	1N HBr	1 h	23.213	0.023	15.965	0.017	43.353	0.049	0.978	0.958
MUP0 115-223.5	Tau Pit	Penhalonga Fm.	4N HBr	3 h	20.444	0.046	15.698	0.036	44.115	0.103	0.990	0.985
MUP0 115-223.5	Tau Pit	Penhalonga Fm.	8.8N HBr	6 h	26.412	0.268	16.400	0.167	43.874	0.447	0.995	0.987
MUP0 115-223.5	Tau Pit	Penhalonga Fm.	8.8N HBr	17 h	21.070	0.138	15.732	0.089	36.580	0.208	0.991	0.993
MUP0 115-223.5	Tau Pit	Penhalonga Fm.	HF conc.	17 h	24.116	0.049	16.190	0.033	35.333	0.075	0.988	0.979
MUP0 115-223.5	Tau Pit	Penhalonga Fm.	HF conc.	96 h	18.716	0.045	15.657	0.039	37.592	0.094	0.984	0.982
MUP0 115-237.5	Tau Pit	Penhalonga Fm.	mix	30 min	16.911	0.217	15.398	0.199	36.894	0.475	0.995	0.995
MUP0 115-237.5	Tau Pit	Penhalonga Fm.	1N HBr	1 h	16.842	0.042	15.273	0.039	37.400	0.096	0.988	0.986
MUP0 115-237.5	Tau Pit	Penhalonga Fm.	4N HBr	3 h	19.243	0.068	15.640	0.056	40.185	0.145	0.991	0.989
MUP0 115-237.5	Tau Pit	Penhalonga Fm.	8.8N HBr	6 h	24.900	0.383	16.259	0.251	36.960	0.571	0.996	0.995
MUP0 115-237.5	Tau Pit	Penhalonga Fm.	8.8N HBr	17 h	40.937	0.684	18.296	0.306	38.588	0.645	0.998	0.998
MUP0 115-237.5	Tau Pit	Penhalonga Fm.	HF conc.	17 h	39.737	0.044	18.157	0.021	37.129	0.046	0.978	0.963
MUP0 115-237.5	Tau Pit	Penhalonga Fm.	HF conc.	96 h	18.731	0.106	15.690	0.090	37.855	0.217	0.992	0.994

[a] Errors are two standard deviations absolute (Ludwig, 2003).
[b] r_1 = $^{206}Pb/^{204}Pb$ vs. $^{207}Pb/^{204}Pb$ error correlation (Ludwig, 2003).
[c] r_2 = $^{206}Pb/^{204}Pb$ vs. $^{208}Pb/^{204}Pb$ error correlation (Ludwig, 2003).

Table 5
Pb isotope data of sulfides from sedimentary rocks associated with BIFs in the Tau pit (TGB)

Sample	Locality/area	Formation (Fm.)	Mineral	$^{206}Pb/^{204}Pb$	±2σ[a]	$^{207}Pb/^{204}Pb$	±2σ[a]	$^{208}Pb/^{204}Pb$	±2σ[a]	r_1[b]	r_2[c]
MUP0 34-238.5 A	Tau Pit	Penhalonga Fm.	Arsenopyrite	14.249	0.007	15.009	0.009	33.947	0.025	0.961	0.920
MUP0 34-238.5 B	Tau Pit	Penhalonga Fm.	Arsenopyrite	14.250	0.006	15.010	0.009	33.955	0.047	0.967	0.487
MUP0 115-185 A	Tau Pit	Penhalonga Fm.	Arsenopyrite	14.553	0.008	15.056	0.010	34.040	0.027	0.958	0.928
MUP0 115-185 B	Tau Pit	Penhalonga Fm.	Arsenopyrite	14.443	0.008	15.073	0.010	34.091	0.028	0.966	0.920
MUP0 115-194 A	Tau Pit	Penhalonga Fm.	Arsenopyrite	14.094	0.007	14.995	0.009	33.788	0.027	0.963	0.900
MUP0 115-194 B	Tau Pit	Penhalonga Fm.	Arsenopyrite	14.134	0.007	15.026	0.009	33.876	0.026	0.956	0.924
MUP0 34-238.5	Tau Pit	Penhalonga Fm.	Pyrrhotite	14.418	0.007	15.026	0.009	34.126	0.026	0.962	0.933
MUP0 115-185	Tau Pit	Penhalonga Fm.	Pyrrhotite	14.487	0.008	15.047	0.010	34.083	0.027	0.959	0.938
MUP0 115-194	Tau Pit	Penhalonga Fm.	Pyrrhotite	14.223	0.007	15.006	0.009	33.949	0.025	0.967	0.937
MUP0 115-256	Tau Pit	Penhalonga Fm.	Pyrrhotite	13.942	0.006	14.907	0.009	33.674	0.025	0.961	0.908
Mupane galena	Tau Pit	Penhalonga Fm.	Galena	13.972	0.008	14.955	0.011	33.634	0.028	0.963	0.933

[a] Errors are two standard deviations absolute (Ludwig, 2003).
[b] r_1 = $^{206}Pb/^{204}Pb$ vs. $^{207}Pb/^{204}Pb$ error correlation (Ludwig, 2003).
[c] r_2 = $^{206}Pb/^{204}Pb$ vs. $^{208}Pb/^{204}Pb$ error correlation (Ludwig, 2003).

PbSL on garnet separates followed the procedure presented by Frei and Kamber (1995) with modifications in acid strengths and reaction times (see details in Table 4). Chemical separation of Pb from whole rocks, sulfides and step-leach solutions was performed over conventional glass stem and subsequently miniature glass stem anion exchange columns containing, respectively, 1 ml and 200 µl 100–200 mesh Bio-Rad AG 1 × 8 resin. Pb was analyzed in a static multi-collection-mode where fractionation was controlled by repeated analysis of the NBS 981 standard (using values of Todt et al. (1993)). The average fractionation amounted to 0.105 ± 0.008% (2σ, n = 5) per atomic mass unit. Total procedural blanks remained below <200 pg Pb which compared to >100 ng Pb loads, insignificantly affected the measured Pb isotopic ratios of the samples.

4. Results

4.1. REE and yttrium

Analyses of selected trace elements, including Ge, plus the major oxides for individual mesobands of BIFs, volcanic and sedimentary rocks from the TGB are presented in Table 1. The BIF groups are listed according to locality. Rare earth + yttrium (REY) patterns of individual mesobands are presented with Y fitted between Dy and Ho in accordance with their decreasing ionic radius (Bau and Dulski, 1996). REY patterns are normalized against Post Archean Australian Shale (PAAS; Taylor and McLennan (1985). Gadolinium concentrations were calculated from neighboring REEs using the relationship Gd = 1/3 × Sm + 2/3 × Tb, in order to circumvent the problem with unidentified isobaric interferences on the measured ^{152}Gd peak.

BIF REY_{PAAS} patterns (Fig. 6A–C) are characterized by depletion of light and middle REE relative to heavy REE (subsequently LREE, MREE and HREE) with Pr/Yb_{PAAS} = 0.21–0.82 and Pr/Sm_{PAAS} = 0.48–0.82 (Table 2). All BIFs show positive La_{PAAS} anomalies (extrapolated from Pr and Nd in order to eliminate possible Ce anomalies using the formula of Bolhar et al. (2004) and pronounced positive Eu anomalies (Eu/Eu^*_{PAAS} = 1.87 – 4.02). Yttrium is significantly enriched relatively to Ho in all mesobands, yielding strongly superchondritic Y/Ho ratios (average BIF sample values ranging from 30–41 (Table 2); chondritic Y/Ho ratio = ~28). The behavior of Ce is diverse with small negative and positive anomalies (Table 2); an exception is sample SH 41 G with a high Ce/Ce_{PAAS} value of 1.63. Variations in REY patterns are mostly attributed to the major element composition of respective mesobands (cf. Tables 1 and 2). For example, in sample MUPD 024 (Fig. 6D), the SiO_2-rich horizons "A" and "C" show flatter MREE-HREE patterns compared to neighboring Fe_2O_3-rich bands "B" and "D".

4.2. Pb isotopes

Pb isotopic ratios obtained from individual BIF mesobands and associated volcanic and sedimentary rocks are listed in Table 3 together with corresponding Pb, U and Th concentrations for some of the samples. PbSL isotopic ratios on garnet separates obtained from drill core samples (MUPD 34-156, MUPD 115-223.5 and MUPD 115-237.5) from the Mupane mine (Tau pit) are presented in Table 4. Table 5 contains Pb isotopic ratios from secondary metamorphic sulfides in sedimentary rocks associated with the BIFs in the Mupane mine.

BIF mesoband data are plotted in conventional common Pb isotope diagrams (Fig. 7 A and B) which contain the two-stage evolution curve for average crustal Pb (Stacey and Kramers, 1975) and the average Archean mantle growth curve (Kramers and Tolstikhin, 1997) for reference purposes. In Fig. 7A, the BIF data each delineate own, relatively well-defined trajectories that roughly plot between the two reference growth curves. Regression through all BIF data points results in an imprecisely defined correlation line with a slope corresponding to an age of 2.73 ± 0.15 Ga (MSWD = 54; not plotted), which encompasses the inferred depositional age of the TGB BIFs. The individual trend lines of the five BIFs studied here are distinctly separated from each other, both with respect to their overall $^{206}Pb/^{204}Pb$, $^{207}Pb/^{204}Pb$ and $^{208}Pb/^{204}Pb$ ranges and relative positions in the respective uranogenic and uranogenic-thorogenic common lead spaces (Fig. 7A and B). This is most characteristic in the uranogenic versus thorogenic diagram (Fig. 7 B). Two BIF trends can be distinguished in Fig. 7A. The first trend, defined by samples from Jim's Luck, Matsiloje and Signal Hill plots at lower $^{207}Pb/^{204}Pb$ ratios relative to given $^{206}Pb/^{204}Pb$ ratios, compared to the two other BIFs (Tau and Tholo pits of the Mupane mine) which plot close to the Stacey and Kramers (1975) growth curve. Additionally the trajectories defined by mesobands of the Mupane BIFs (Tau pit and Tholo pit; Fig. 7A) are flatter than the trend lines with slopes corresponding to ~2.7 Ga defined by the other BIFs studied here. The slopes of these flatter trajectories correspond to ~2.0 Ga trajectories in this diagram and are compatible with ~2.0 Ga reference line also defined by PbSL data of garnet and bulk sulfides from this location (see below).

PbSL data of garnet fractions from three sedimentary rocks associated with the Tau BIF are plotted in conventional Pb isotope diagrams in Fig. 8A and B. In Fig. 8A, a combined regression through the garnet data points defines a correlation line with a slope corresponding to an apparent age of 1976 ± 88 Ma (MSWD = 48). In Fig. 8B, the garnet data define two different trends which are characterized by high inferred Th/U ratios (denoted monazite), and low inferred Th/U ratios (denoted zircon), respectively. Such trends are thought to originate from the combined contribution of thorogenic and uranogenic Pb from microscopically small inclusions of monazite and zircon, respectvely (e.g., Schaller et al., 1997).

Fig. 9A and B show the Pb isotope data of sulfides from sedimentary rocks associated with the Tau BIFs. For comparative purposes, the reference line defined by PbSL data of garnets from Fig. 8A is plotted in Fig. 9A, and so are the data points of individual mesobands of the Tau BIF. As a reference, Fig. 9A and B show Pb isotopic ratios of BIF mesobands corrected back to 2.7 Ga using U and Pb concentrations (see Table 3). The garnet reference line in Fig. 8A, although imprecisely defined, intersects the Stacey and Kramers (1975) Pb evolution curve in the vicinity of the Tau BIF data and implies that the BIFs in the Mupane mine incorporated an isotopically similar Pb to that reflected by the associated sedimentary rocks in this deposit. Because of the overlap of data fields (Fig. 9A), this is also true for the leads typical of gold-bearing sulfides (arsenopyrite, pyrrhotite and galena) which are hosted by these BIFs and other sedimentary rocks at this location. The Pb isotope composition of the one galena sample lies at the lower left end of the sulfide and BIF mesoband data fields (Fig. 9A and B) and implies a prehistory of the source leads in a reservoir characterized by higher μ-values than average continental crustal Pb at about the ~2.7 Ga deposition age of the sediments.

4.3. Ge–Si–Fe relationships and Sm–Nd isotopes

Ge/Si ratios versus SiO_2 (data in Table 1) from the TGB BIFs show a hyperbolic (mixing) relationship overlapping with that depicted by the ~2.45 Ga old Hamersley BIF, Western Australia (Hamade et al., 2003; Fig. 10). This relationship is defined by increasing Si content accompanied by decreasing Ge/Si ratios (Fig. 10), or by increasing Fe concentrations accompanied by increasing Ge/Si (not shown). Fig. 10 also shows the Ge/Si versus SiO_2 relationship of BIFs

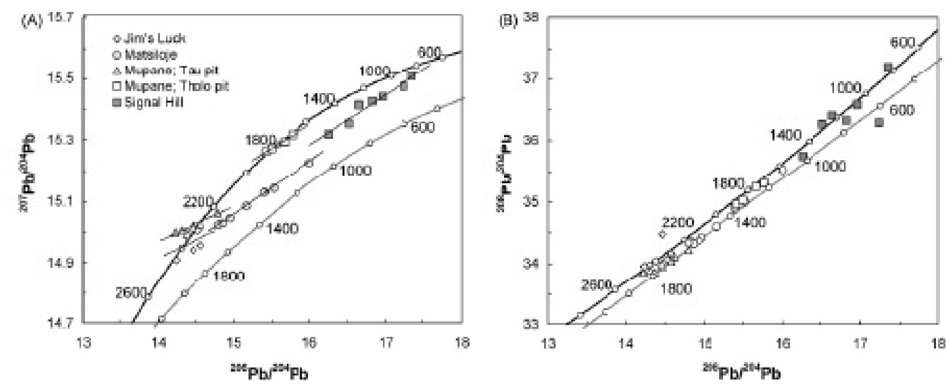

Fig. 7. Uranogenic (A) and thorogenic–uranogenic (B) common Pb isotope diagrams for BIFs reported herein (data in Table 3). In (A) BIF mesoband samples define individual trajectories. BIFs from the Mupane mine (Tau and Tholo pits) lie on an elevated $^{207}Pb/^{204}Pb$ relative to $^{206}Pb/^{204}Pb$ trend compared to the BIFs from Jim's Luck, Matsiloje and Signal Hill. This implies subtle differences in the source regions contributing particulate matter to the sedimentary environment of these BIFs. The Mupane mine BIFs have incorporated Pb from sources that, on average, evolved in higher μ ($^{238}U/^{204}Pb$) environments than those contributing Pb to the remaining BIFs. In (B) the BIF data points scatter around a linear trend indicating a rather homogeneous source region with respect to its Th/U signature. The black line is the two-stage evolution curve for average continental crustal Pb of Stacey and Kramers (1975) and the grey line is the average MORB Pb source growth curve of Kramers and Tolstikhin (1997).

from the ~3.7–3.8 Ga Isua Greenstone Belt, W Greenland (Frei and Polat, 2007) for comparative purposes.

Sm–Nd isotopes and concentrations of these elements for individual mesobands of BIFs and associated volcanic and sedimentary rocks from the TGB are presented in Table 6. All the initial ε_{Nd} values of the BIFs and associated rocks are calculated using an age of 2.7 Ga, which is considered a probable depositional age for the TGB BIFs (see above). Mesoband MUPD 024-58 D yielded a geologically meaningless model age as did a repeated sample (see Table 6). At this stage there is no reasonable explanation for this; the subsample has apparently experienced a disturbance in its Sm–Nd systematics. Therefore, the Sm–Nd isotope data of this sample is excluded from the results and discussion sections below. However, it is important to stress that due to very low REE concentrations in some of the studied BIFs, long-term parent–daughter disturbances are likely to be facilitated, as also observed in BIFs from other studies (e.g., Bau, 1993; Bau and Dulski, 1992; Frei et al., 1999).

Neodymium and Sm concentrations in the studied TGB BIFs range from 0.20 to 5.36 ppm (average 1.31 ± 1.13 ppm, 1σ, n = 31) and from 0.05–1.25 ppm (average 0.30 ± 0.26 ppm, 1σ, n = 31), respectively (Table 6). $^{143}Nd/^{144}Nd$ ratios are relatively uniform defining an average subchondritic value of ~0.5115 (Table 6). There is, in contrast, some variation in the Sm/Nd ratios (range of $^{147}Sm/^{144}Nd$ from 0.119–0.152, Table 6). The above signatures translate into Nd model ages (T_{DM}) ranging from 2.76 to 3.69 Ga (average 3.22 ± 0.21 Ga, 1σ, n = 31) and a corresponding range in ε_{Nd} (t = 2700 Ma) values of −3.74 to +3.70, thus indicating depleted and enriched sources for the BIFs.

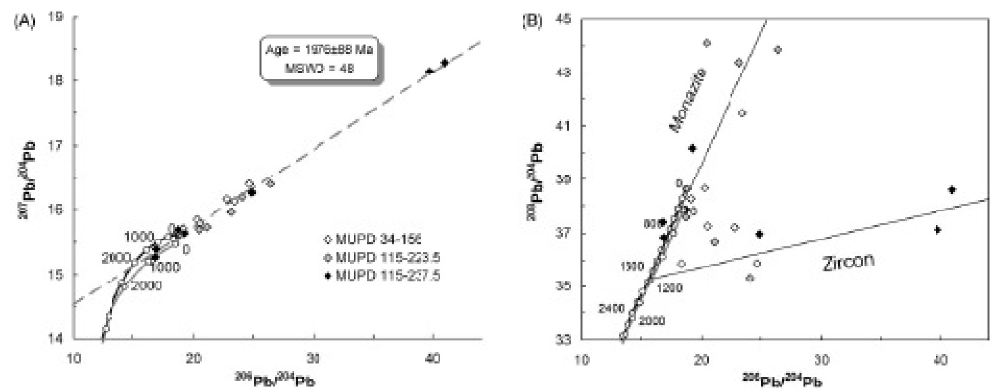

Fig. 8. Uranogenic (A) and thorogenic-uranogenic (B) common Pb isotope diagrams with PbSL data on garnet separates from drill cores MUPD 34 and 155 from the Tau pit in the Mupane mine (data in Table 4). In (A) the combined correlation line defined by these data points has a slope corresponding to an apparent age of 1976 ± 88 Ma (MSWD = 48). This age is, at least for the Mupane mine area, interpreted as a tectono-metamorphic age that can be correlated with major tectono-metamorphic events within the adjacent Limpopo Mobile Belt. In (B) the garnet PbSL data define two trends: one characterized by high $^{208}Pb/^{204}Pb$ relative to $^{206}Pb/^{204}Pb$ ratios and the other by high $^{206}Pb/^{204}Pb$ and low $^{208}Pb/^{204}Pb$ ratios. These trends are interpreted to result from Pb derived from monazite and zircon inclusions, respectively (see text for details). The black line is the two-stage evolution curve for average continental crustal Pb of Stacey and Kramers (1975) and the grey line is the average MORB Pb source growth curve of Kramers and Tolstikhin (1997).

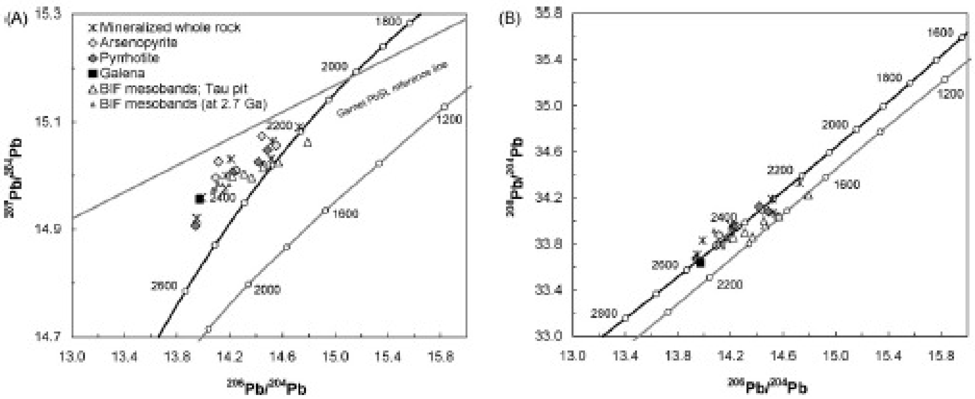

Fig. 9. Uranogenic (A) and thorogenic-uranogenic (B) common Pb isotope diagrams with data from whole rocks, sulfides, BIF mesobands and 2.7 Ga age-corrected BIF mesobands from the Mupane mine drill cores MUPD 34 and 115 (data in Tables 3, 4 and 5). The garnet PbSL reference line (see Fig. 8A) is inserted for comparative purposes. The black line is the two-stage evolution curve for average continental crustal Pb of Stacey and Kramers (1975) and the grey line is the average MORB Pb source growth curve of Kramers and Tolstikhin (1997). In (A) the majority of data points, including the one for galena, lie above the two Pb growth curves implying a prehistory of the source leads in a reservoir characterized by higher μ-values than average continental crustal Pb at about the ~2.7 Ga deposition age of the sediments. The overlap in data arrays defined by both clastic and chemical sediments in the Tau drill cores implies that the erosional products contributing to the respective Pb isotopic compositions were fairly homogeneous during the deposition period of the Tau sedimentary rocks (see text for discussion).

The Sm–Nd isotope data of volcanic rocks from the Lady Mary Formation and Penhalonga Formation (Table 6) are clearly different in that the initial ε_{Nd} values are positive (+1.6 ± 1.0, 1σ, n = 5) for the volcanic rocks of the Lady Mary Formation, whereas they are negative (−1.3 ± 0.5, 1σ, n = 6) for those of the Penhalonga Formation, indicating formation from depleted and enriched mantle sources, respectively. The Nd T_{DM} ages defined by the Lady Mary Formation and Penhalonga Formation volcanic rocks are indistinguishable from each other (both average values ~3.3 Ga, Table 6) and compare well with the average (~3.2 Ga) T_{DM} ages defined by the associated BIFs and by the sedimentary rocks (Table 6). The Sm–Nd isotope data of BIFs and associated volcanic rocks plot along a correlation line in a conventional isochron diagram (Fig. 11) with a slope corresponding to an apparent age of 2956 ± 250 Ma (MSWD = 6.4). The initial ε_{Nd} value defined by this line is +0.5 (Fig. 11). The correlation line represents a mixing line, essentially defined by a high Sm/Nd–high ^{143}Nd/^{144}Nd (depleted mantle) and a low Sm/Nd–low ^{143}Nd/^{144}Nd (continental crustal) end-member. The volcanic rocks of the Penhalonga Formation plot in an intermediate position and at the high Sm/Nd–high ^{143}Nd/^{144}Nd end of the data array defined by the BIFs (Fig. 11). Data points of sedimentary rocks scatter along the correlation line, with the most unradiogenic values defining the continental crustal end-member (Fig. 11).

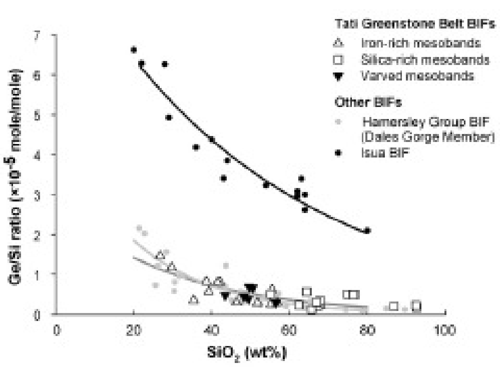

Fig. 10. Diagram showing the relationship between SiO_2 (wt%) versus Ge/Si ratios for individual mesobands from the TGB BIFs. Data define a hyperbolic trend (dark grey curve) where one end-member is controlled by input of hydrothermal fluids and the other by continentally derived solutes. Data imply a similar two-source iron and silica decoupling as reported for the Proterozoic Hamersley BIF (Hamade et al., 2003): data array shown by light grey dots and light grey curve. Black dots modeled by the black curve depict the data array of BIF mesobands from the Isua Greenstone Belt (W Greenland; Frei and Polat, 2007). The Isua BIF hyperbolic trend plots at elevated Ge/Si ratios relative to the TGB and Hamersley BIFs (see text for details).

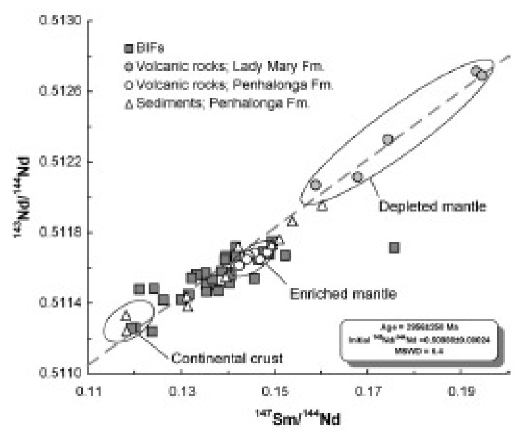

Fig. 11. Sm–Nd isochron diagram with data for BIFs, associated volcanic and sedimentary rocks from the TGB. The correlation line has a slope which corresponds to an apparent age of 2956 ± 250 Ma (MSWD = 6.4) and defines an initial ε_{Nd} value of +0.51. The line is interpreted as a mixing line between contributions from depleted mantle-like material (characterized by volcanic rocks from the Lady Mary Formation) and continentally derived sources (characterized by clastic sedimentary rocks of the Penhalonga Formation); see text for details.

Table 6

Sm–Nd concentrations and isotopic data of BIFs and associated volcanic and sedimentary rocks from the TGB.

Sample	Locality/area	Formation (Fm.)	Rock type/mesoband	Sm (ppm)	Nd (ppm)	$^{147}Sm/^{144}Nd$[a]	$^{143}Nd/^{144}Nd$[b]	$\pm 2\sigma_m$ abs.	T_{DM}[c]	T_{CHUR}[d]	$\varepsilon_{Nd}(0)$	Age (Ma)	ε_{Nd}(age)
BIFs													
Jims Ba A	Jim's Luck	Matsloje Fm.	Oxide BIF/Fe	0.67	2.88	0.14041	0.511513	7	3.42	3.03	−21.94	2700	−1.40
Jims Ba B	Jim's Luck	Matsloje Fm.	Oxide BIF/Si	0.33	1.44	0.13796	0.511477	14	3.38	2.99	−22.66	2700	−1.26
Jims Ba C	Jim's Luck	Matsloje Fm.	Oxide BIF/Fe	0.42	1.86	0.13610	0.511500	12	3.25	2.85	−22.21	2700	−1.16
Jims Ba D	Jim's Luck	Matsloje Fm.	Oxide BIF/Varv	0.36	1.74	0.12376	0.511239	12	3.25	2.91	−27.29	2700	−1.96
Jims Ba E	Jim's Luck	Matsloje Fm.	Oxide BIF/Varv	0.18	0.86	0.12419	0.511482	9	2.85	2.40	−22.55	2700	2.66
							Average		3.23				−1.02
							$\pm 1\sigma$		0.20				1.89
MAT 3C-A	Matsloje	Matsloje Fm.	Oxide BIF/Si	0.11	0.52	0.13525	0.511504	10	3.21	2.80	−22.12	2700	−0.77
MAT 3C-B	Matsloje	Matsloje Fm.	Oxide BIF/Fe	0.13	0.62	0.14020	0.511574	12	3.28	2.85	−20.75	2700	−1.12
MAT 3C-C	Matsloje	Matsloje Fm.	Oxide BIF/Fe	0.10	0.43	0.14651	0.511646	21	3.43	2.99	−19.35	2700	−1.92
MAT 3C-D	Matsloje	Matsloje Fm.	Oxide BIF/Si	0.07	0.34	0.12027	0.511421	[illegible]	3.16	2.72	−23.75	2700	[illegible]
MAT 3C-E	Matsloje	Matsloje Fm.	Oxide BIF/Varv	0.09	0.36	0.14893	0.511675	23	3.48	3.05	−18.78	2700	−2.19
MAT 3C-F	Matsloje	Matsloje Fm.	Oxide BIF/Si	0.06	0.29	0.12037	0.511261	9	3.09	2.71	−26.86	2700	−0.23
MAT 3C-G	Matsloje	Matsloje Fm.	Oxide BIF/Fe	0.12	0.55	0.13796	0.511470	7	3.40	3.01	−22.79	2700	−1.39
MAT 3C-H	Matsloje	Matsloje Fm.	Oxide BIF/Si	0.09	0.45	0.11627	0.511258	14	3.07	2.77	−26.93	2700	−0.02
MAT 3C-K	Matsloje	Matsloje Fm.	Oxide BIF/Varv	0.21	0.90	0.13542	0.511466	15	3.29	2.90	−22.85	2700	−1.57
							Average		3.27				−1.20
							$\pm 1\sigma$		0.14				0.82
Tau 20 A	Tau Pit	Penhalonga Fm.	Oxide BIF/Si	0.23	1.03	0.13333	0.511562	24	3.02	2.57	−20.98	2700	1.05
Tau 20 B	Tau Pit	Penhalonga Fm.	Oxide BIF/Si	0.10	0.44	0.13161	0.511448	7	3.17	2.77	−23.21	2700	−0.60
Tau 20 C	Tau Pit	Penhalonga Fm.	Oxide BIF/Fe	0.30	1.32	0.13671	0.511534	20	3.21	2.79	−21.54	2700	−0.70
Tau 20 D	Tau Pit	Penhalonga Fm.	Oxide BIF/Si	0.11	0.47	0.14569	0.511539	9	3.63	3.22	−21.44	2700	−3.74
Tau 20 E	Tau Pit	Penhalonga Fm.	Oxide BIF/Fe	0.20	0.90	0.13008	0.511668	24	3.07	2.61	[illegible]	2700	0.87
Tau 20 F	Tau Pit	Penhalonga Fm.	Oxide BIF/Fe	0.37	1.79	0.12621	0.511419	12	3.03	2.62	−23.79	2700	0.71
Tau 20 G	Tau Pit	Penhalonga Fm.	Oxide BIF/Si	0.21	0.86	0.14951	0.511750	8	3.34	2.85	−17.31	2700	−0.91
							Average		3.21				−0.47
							$\pm 1\sigma$		0.20				1.53
MURD 024-58 A	Trojan Pit	Penhalonga Fm.	Oxide BIF/Si	0.05	0.20	0.13938	0.511645	8	3.10	2.63	−19.38	2700	0.55
MURD 024-58 B	Trojan Pit	Penhalonga Fm.	Oxide BIF/Fe	0.16	0.67	0.14069	0.511556	5	3.34	2.92	−21.10	2700	−1.65
MURD 024-58 C	Trojan Pit	Penhalonga Fm.	Oxide BIF/Si	0.05	0.20	0.14166	0.511720	8	3.04	2.53	−17.92	2700	1.22
MURD 024-58 D	Trojan Pit	Penhalonga Fm.	Oxide BIF/Fe	0.16	0.55	0.17819	0.511625	66	6.57	8.11	−19.77	2700	−11.43
MURD 024-58 D[e]	Trojan Pit	Penhalonga Fm.	Oxide BIF/Fe	0.16	0.55	0.17580	0.511714	7	5.80	6.63	−18.02	2700	−10.83
							Average		3.16				0.04
							$\pm 1\sigma$		0.13				1.22
SH-41 A	Signal Hill	Unknown stratigraphic position	Oxide BIF/Varv	1.25	5.36	0.14162	0.511664	4	3.15	2.63	−19.00	2700	0.14
SH-41 B	Signal Hill	Unknown stratigraphic position	Oxide BIF/Fe	0.63	2.89	0.13225	0.511542	7	3.02	2.58	−21.38	2700	1.02
SH-41 C	Signal Hill	Unknown stratigraphic position	Oxide BIF/Si	0.56	2.43	0.13865	0.511579	9	3.20	2.77	−20.65	2700	−0.48
SH-41 D	Signal Hill	Unknown stratigraphic position	Oxide BIF/Fe	0.44	1.69	0.13528	0.511572	10	3.08	2.63	−20.79	2700	0.56
SH-41 E	Signal Hill	Unknown stratigraphic position	Oxide BIF/Si	0.44	1.76	[illegible]	0.511670	14	3.64	3.07	−18.00	2700	−2.48

Table 6 (*Continued*)

Sample	Locality/area	Formation (Fm.)	Rock type/mesoband	Sm (ppm)	Nd (ppm)	$^{147}Sm/^{144}Nd$[a]	$^{143}Nd/^{144}Nd$[b]	$\pm 2\sigma_m$ abs.	T_{DM}[c]	T_{CHUR}[d]	$\varepsilon_{Nd}(0)$	Age (Ma)	ε_{Nd}(age)
SH-41 F	Signal Hill	Unknown stratigraphic position	Oxide BIF/Fe	0.59	2.93	0.12106	0.511479	5	2.76	2.33	−22.61	2700	3.70
SH-41 G	Signal Hill	Unknown stratigraphic position	Oxide BIF/Si	0.51	2.08	0.14763	0.511690	10	3.38	2.93	−18.50	2700	−1.46
							Average		3.18				0.00
							$\pm 1\sigma$		0.27				2.06
Volcanic rocks													
LM 46	Lady Mary Farm	Lady Mary Fm.	Basalt	2.65	10.62	0.16787	0.512114	4	3.46	2.75	−10.22	2700	−0.20
MAND 001-67	Map Nora	Lady Mary Fm.	Basalt	3.52	12.22	0.17440	0.512326	5	3.21	2.12	−6.08	2700	1.68
MAND 001-96.5	Map Nora	Lady Mary Fm.	Basalt	2.19	6.84	0.19336	0.512713	5	3.28	−3.48	1.47	2700	2.65
MAND 001A-16	Map Nora	Lady Mary Fm.	Basalt	2.34	7.28	0.19454	0.512690	3	3.67	−3.72	1.01	2700	1.78
GOED 002-45	Golden Eagle	Lady Mary Fm.	Basalt	1.38	5.25	0.15892	0.512069	3	3.02	2.26	−11.11	2700	2.04
							Average		3.33				1.59
							$\pm 1\sigma$		0.22				0.96
PEN 43	Selkirk	Penhalonga Fm.	Basalt	2.19	9.02	0.14687	0.511649	3	3.44	3.01	−19.30	2700	−1.99
MURD 024-80	Trojan Pit	Penhalonga Fm.	Basalt	2.06	8.38	0.14848	0.511688	4	3.43	2.98	−18.53	2700	−1.79
MURD 024-183.8	Trojan Pit	Penhalonga Fm.	Basalt	2.72	11.30	0.14574	0.511686	4	3.30	2.83	−18.57	2700	−0.86
MURD 115-327.5	Tau Pit	Penhalonga Fm.	Basalt	2.15	9.13	0.14252	0.511614	4	3.30	2.86	−19.98	2700	−1.16
MURD 340-30	Owena Pit	Penhalonga Fm.	Basalt	2.40	10.06	0.14438	0.511671	5	3.26	2.80	−18.86	2700	−0.68
MURD 369-356	Tau Pit	Penhalonga Fm.	Basalt	2.50	10.51	0.14412	0.511648	4	3.30	2.85	−19.31	2700	−1.05
							Average		3.34				−1.26
							$\pm 1\sigma$		0.07				0.48
Sedimentary rocks													
PEN 58	Selkirk	Penhalonga Fm.	Garnet-chert	2.45	12.57	0.11830	0.511331	4	2.81	2.52	−25.50	2700	1.83
PEN 59	Selkirk	Penhalonga Fm.	Garnet-chlorite-chert	[illegible]	15.00	0.14201	0.511714	4	3.07	2.56	−17.92	2700	0.99
MURD 34-238.5	Tau Pit	Penhalonga Fm.	Sulfide-bearing quartz-grunerite-siderite-chert	2.71	10.84	0.15104	0.511761	5	3.39	2.81	−17.10	2700	−1.24
MURD 115-76.5	Tau Pit	Penhalonga Fm.	Conglomerate	3.18	16.26	0.11823	0.511241	3	3.06	2.70	−27.25	2700	0.02
MURD 115-185	Tau Pit	Penhalonga Fm.	Sulfide-bearing quartz-grunerite-siderite-chert	0.28	1.07	0.16024	0.511956	14	3.42	2.83	−13.30	2700	−0.64
MURD 115-194	Tau Pit	Penhalonga Fm.	Quartz-grunerite-siderite-BIF	0.56	2.25	0.14948	0.511733	8	3.38	2.90	−17.66	2700	−1.25
MURD 115-223.5	Tau Pit	Penhalonga Fm.	Garnet-bearing graphite-chert	0.56	2.58	0.13120	0.511437	7	3.18	2.78	−23.42	2700	−0.67
MURD 115-276.5	Tau Pit	Penhalonga Fm.	Quartz-grunerite-siderite-chert	0.14	0.55	0.15389	0.511863	8	3.29	2.74	−15.11	2700	−0.24
MURD 115-286	Tau Pit	Penhalonga Fm.	Garnet-bearing graphite-chert	1.45	6.69	0.13139	0.511382	7	3.29	2.91	−24.50	2700	−1.81
MURD 115-361.5	Tau Pit	Penhalonga Fm.	Garnet-bearing graphite-chert	2.34	10.16	0.13952	0.511549	7	3.30	2.88	−21.24	2700	−1.38
							Average		3.23				−0.44
							$\pm 1\sigma$		0.16				1.08

Fe = Fe-rich bands; Si = Si-rich bands; Varv = Varved bands.

[a] Uncertainty is less than 0.2%.

[b] Measured $^{143}Nd/^{144}Nd$ ratio corrected for mass fractionation using $^{146}Nd/^{144}Nd$ = 0.7219.

[c] Refers to the depleted mantle model of DePaolo (1981).

[d] Refers to 0.1 permil deviations from Chondritic Uniform Reservoir ($^{143}Nd/^{144}Nd$ = 0.512638).

[e] Repeated sample.

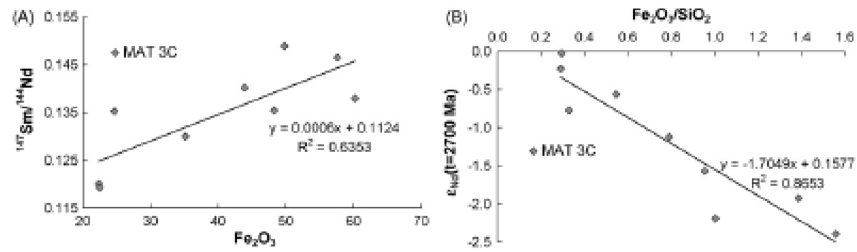

Fig. 12. Diagram showing the relationships in mesobands from sample MAT-3C (data in Tables 1 and 6) between Fe_2O_3 concentrations versus $^{147}Sm/^{144}Nd$ ratios (A) and Fe_2O_3/SiO_2 ratios and $\varepsilon_{Nd}(t = 2700\ Ma)$ values (B). In (A) the positive correlation between Sm/Nd ratios and Fe concentrations implies a hydrothermal source of Fe. The inverse correlation between Fe_2O_3/SiO_2 ratios and $\varepsilon_{Nd}(t = 2700\ Ma)$ in (B) is capable of characterizing two end-members that control the iron and silicon budget in this BIF. The Fe-rich (hydrothermal) end-member is defined by an extrapolated ε_{Nd} value of −2.5, whereas the Si-rich (continental) end-member can be constrained by an extrapolated ε_{Nd} value of −0.4. These relationships point to an origin of hydrothermal fluids from enriched mantle-like volcanic rocks, and a continental crustal component in the BIF with a likely mafic composition (see text for details).

This mixing relationship in the BIFs is best illustrated in Fig. 12B, where Fe_2O_3/SiO_2 ratios of individual BIF mesobands of sample MAT-3C (data in Tables 1 and 6) are plotted against the respective $\varepsilon_{Nd}(t = 2700\ Ma)$ values. There is an inverse correlation between these two parameters which again illustrates the mixing of two sources. The high Sm/Nd end-member is defined by high Fe_2O_3 concentrations (Fig. 12A). The inverse correlation between Fe_2O_3/SiO_2 and $\varepsilon_{Nd}(t = 2700\ Ma)$ depicted in Fig. 12B allows for a rough characterization of the two end-members in terms of their $\varepsilon_{Nd}(t = 2700\ Ga)$ values: the Fe-rich source is constrained by an end-member with an extrapolated $\varepsilon_{Nd}(t = 2700\ Ma)$ value of −2.5, compared to the Si-rich source with an extrapolated end-member $\varepsilon_{Nd}(t = 2700\ Ma)$ value of −0.4. The implications of this are discussed below.

5. Discussion

The BIFs and associated volcanic and sedimentary rocks of the TGB present an opportunity to evaluate Neoarchean ocean chemistry because fresh drill cores permitted detailed geochemical data. The presented isotopic systematics, as well as the major and trace element data suggest: (1) that the TGB BIFs are consistent with marine chemical sedimentation (precipitation); (2) that an older enriched mantle component contributed to the BIFs; and (3) that a ∼2.0 Ga metamorphic event overprinted the TGB.

5.1. REY systematics of the TGB BIFs

Hydrothermally discharged fluids preferentially scavenge Eu^{2+} by interaction with submarine volcanic rocks, at mid ocean ridges (MOR) and oceanic arcs (German and Von Damm, 2007), and create a gradual enrichment of Eu relative to the remaining REE in the seawater. There is a gradual decrease in the positive Eu anomalies in ancient BIFs from the Archean to the Proterozoic (e.g., Condie, 1997), reflecting the decreasing contribution of high-temperature hydrothermal fluids into the marine environment (e.g., Danielson et al., 1992). The Neoarchean TGB BIFs show pronounced Eu_{PAAS} anomalies, on average $Eu/Eu^* = 2.99 \pm 0.73$ (1σ, $n = 32$; Table 2), indicating that highly reducing high-temperature hydrothermal fluids were an important source for REEs in the ambient seawater (Bau and Dulski, 1996).

The magnitude of Eu_{PAAS} anomalies in the TGB BIFs is comparable to that of other BIFs known to show features of increased hydrothermal activity, such as the ∼2.45 Ga oxide-facies Hamersley BIF. After normalizing to the Hamersley BIF (average Eu/Eu^*_{PASS} value of 1.42; (Alibert and McCulloch, 1993), any deviations >1.0 are indicative of increased high temperature hydrothermal activity. All Hamersley-normalized Eu/Eu^* (denoted Eu/Eu^{**} in Table 2) values for the TGB BIFs are >1 (average 2.10 ± 0.51, 1σ, $n = 32$). The Eu/Eu^*_{PASS} data from the TGB BIFs indicate increased hydrothermal venting into contemporaneous basin waters during the time of their deposition. This observation can be correlated with the known 2.7 Ga event with increased global mantle-plume activity (Condie, 1998; Stein and Hofmann, 1994).

There is a general absence of Ce anomalies in the TGB BIFs. An exception is sample SH 41 G with a high Ce/Ce_{PAAS} value of 1.63, which is tentatively interpreted to have resulted from post-formational addition of Ce(IV) under oxidative conditions (Slack et al., 2007). A few BIFs deposited during the Eo- and Neoarchean eras show strongly negative Ce anomalies with $Ce/Ce^* = 0.1–0.5$ suggesting strongly oxygated oceanic conditions (Kato et al., 2006). Generally, there is a lack of statistically significant Ce anomalies in Archean BIFs, contrary to modern-day chemical sedimentary rocks (e.g., limestones) which show pronounced negative Ce anomalies (Webb and Kamber, 2000). The lack of negative Ce anomalies in the TGB BIFs implies that redox levels in contemporaneous basin waters during the deposition of these BIFs were lower than those observed in modern marine systems, a feature which has been discussed by many authors in terms of the oxidation history on the Earth's surface (e.g., Derry and Jacobsen, 1990; Fryer, 1977).

Fig. 13 compares the average PAAS-normalized REY patterns of the five TGB BIFs studied here to that of modern seawater, whereas in Fig. 14 an average TGB BIF REY pattern is compared to patterns of other Eoarchean to Paleoproterozoic BIFs. Except for the patterns recently published by Alexander et al. (2008) for the ∼2.9 Ga Pongola BIFs (South Africa), which show variable, slightly depleted HREE patterns (Fig. 14), the TGB BIFs show striking similarities to both seawater and other worldwide BIFs from which complete REY data are available. The magnitude of the positive Eu anomaly of the TGB BIFs compares well with other BIFs, but particularly with those deposited at ∼2.6 to 2.7 Ga which also show elevated Eu/Eu^* values. In order to validate the influence of ancient hydrothermal fluxes, present-day high-T venting fluids may serve as an analogue. Using the conservative mixing calculations applied by Alexander et al. (2008) to model Eu anomalies (taking the Eu/Sm values as proxies for the magnitude of Eu anomalies; their Fig. 6A) in BIFs, approximately 0.1% of a hydrothermal fluid is capable of explaining the magnitude of the Eu anomaly in the TGB BIFs. This is within the usual range capable of explain the Eu/Sm ratios in a variety of Archean BIFs (Alexander et al., 2008; Klein and Beukes, 1989). In fact this value is at the high end of the range and compatible with, for example, the inferred contribution of hydrothermal fluids necessary to explain the elevated Eu

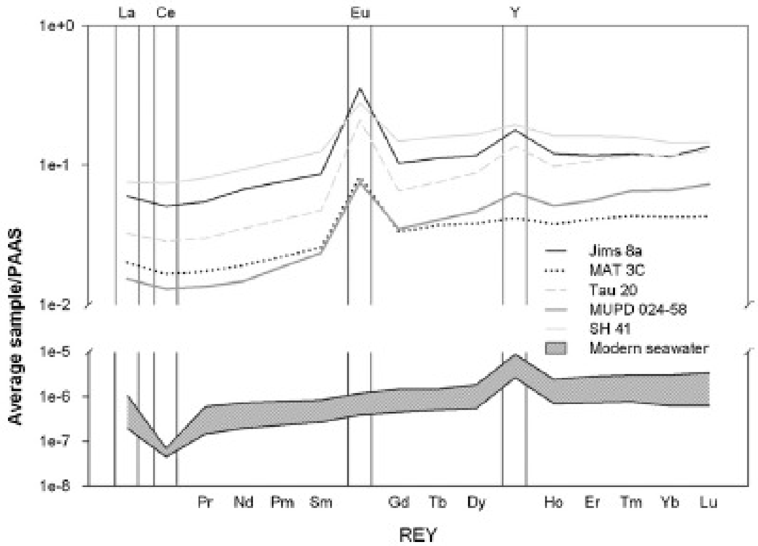

Fig. 13. REY diagrams for the TGB BIFs (average values for the five individual BIFs from this article) compared to modern seawater (REY data from Alibo and Nozaki (1999)). With the exception of Eu and Ce anomalies, the overall REY_{PAAS} patterns of the five TGB BIFs are strikingly similar to modern seawater. This implies that REY contributions to the seawater and respective removal process of these elements in the Archean were similar to modern mechanisms. For details, refer to text.

anomalies of the similarly old Atlantic City BIFs (Wyoming; Frei et al., 2008) and the Eoarchean Isua BIFs (Bolhar et al., 2004; Frei and Polat, 2007).

Y/Ho ratios provide constraints on the depositional environment. Modern seawater is characterized by Y/Ho ratios between 44 and 74 (Bau, 1996). These ratios are substantially higher than the vast majority of geologic materials, including upper crustal rocks and clastic sediments (Rudnick and Gao, 2004) with Y/Ho ratios of ~28 (the average CI Chondrite value; Anders and Grevesse, 1989). Elevated Y/Ho ratios relative to chondrite are characteristic of aqueous systems, and are relevant to seawater (Nozaki et al., 1997) where it is thought that dissolved Ho adsorbs more effectively to particulate matter (including iron oxyhydroxides) than Y (Bau, 1999). The fact that Y/Ho ratios of TGB BIFs are compatible with values in modern seawater implies that, even though the seawater during the TGB depositional period was fertilized by an increased subaqueous hydrothermal venting input (with a likely Y/Ho ratio of ~28; Bau and Dulski, 1999), the average TGB seawater Y/Ho ratio was not significantly depressed. This in turn implies an effective removal mechanism of Ho that could not have been significantly different from today's processes. However, the notion of Alexander et al. (2008) that, if preferential adsorption processes for Ho onto iron oxyhydroxide particles were operating and if these had reached equilibrium with the surrounding water column, then subchondritic Y/Ho ratio would be expected to be characteristic of BIFs in general. The fact that Archean marine precipitates, despite otherwise showing REY patterns similar to that of contemporaneous seawater, systematically show suprachondritic Y/Ho ratios might reflect that exchange equilibria were not reached. Though it has not yet been adequately explained why BIFs show REY patterns similar to modern seawater, the salient similarity between REY patterns in marine Archean precipitates and in modern seawater makes it likely that BIFs truly preserve the original REY signal of the water column from which they were deposited (Alexander et al., 2008).

5.2. Inferences for the prehistory of BIF components and sources of mineralizing fluids based on lead isotopes

The Pb isotope data on sulfides and garnets from the Mupane mine reveal a pronounced U–Pb mineral resetting at ~2.0 Ga (compatible with the partial resetting of the Tau BIF mesobands), which is substantially younger than the ~2.7 Ga ages implied by the mesoband data of the other TGB BIFs (see the trajectories in Fig. 7A). This has important implications for the timing of sulfide-gold mineralization in the Mupane district and perhaps in the entire TGB. As shown in Fig. 9A and B, Pb isotopic data from the Tau BIF overlap with the range of data points for volcanic and sedimentary rocks from this location (Table 3), and with data defined by sulfides from within the BIFs, indicating a common source of Pb. The overlap also implies that the mineralizing fluids were essentially in equilibrium with the host rocks and therefore not likely to have been derived from external (magmatic?) sources. Idiomorphic texture of arsenopyrite, in combination with the age constraints from PbSL data on garnet (Fig. 8A), implies that (re-)crystallization of the sulfides took place during strain-free (veining) stages of the ~2.0 Ga tectono-metamorphic event. Metamorphic ages of ~2.0 Ga have been reported from within the Limpopo Mobile Belt (from the Northern Marginal Zone (e.g., Holzer et al., 1998; Kamber et al., 1995) and from the Central Zone (e.g., Berger and Rollinson, 1997; Boshoff et al., 2006; Kreissig et al., 2000), but such ages have not been described from areas north and south of the mobile belt, in regions thought to have remained cratonic since the emplacement of ~2.6–2.7 Ga tonalite suites. The PbSL data show that metamorphic events of Limpopo affinity can be traced into cratonic areas north of the Limpopo Mobile Belt, and might have implications for the tectono-metamorphic history and collision-related prehistory of the Kaapvaal and Zimbabwe cratons. These results are analogous to the observations by Fedo and Eriksson (1996) who, based on structural mapping of areas in the Buhwa greenstone belt in southern Zimbabwe, described effects pointing to crustal

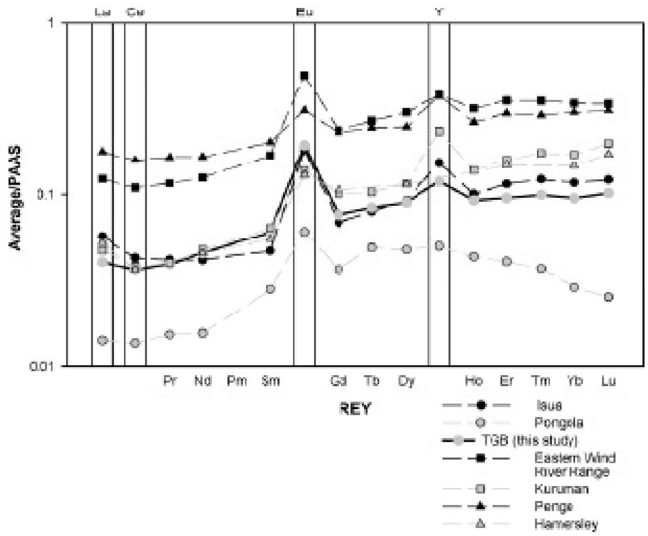

Fig. 14. PAAS-normalized REY diagram comparing average REY patterns from the Tati Greenstone Belt BIFs (this study) with average REY patterns from older and younger oxide facies BIFs from Isua (Frei and Polat, 2007), Pongola (Alexander et al., 2008), Eastern Wind River Range (Frei et al., 2008), Kuruman and Penge (Bau and Dulski, 1996) and Hamersley (Alibert and McCulloch, 1993). With the exception of the Pongola BIF, the PAAS-normalized patterns of Archean BIFs are strikingly similar with HREE enrichment relative to MREE and LREE and positive La, Eu and Y anomalies

shortening that they tentatively associated with Limpopo deformational events. The Buhwa greenstone belt, like the TGB, lies directly adjacent to the Northern Marginal Zone of the Limpopo Belt.

In order to obtain information regarding the ultimate source of Pb in the TGB BIFs, *in situ* age corrections of measured Pb isotope data of mesobands were conducted using U, Th and Pb concentrations obtained by ICP-MS from powder aliquots (values listed in Table 3). *In situ* corrected data are plotted in a common Pb isotope diagram in Fig. 15 together with the data point of the one galena sample from the sulfide mineralization in the Mupane (Tau pit) mine (Table 5). The BIF from Tholo pit differs from the other BIFs by data characterized by higher $^{207}Pb/^{204}Pb$ relative to $^{206}Pb/^{204}Pb$ ratios, and the BIF from Signal Hill by generally more radiogenic signatures compared to the other BIFs studied. This is interpreted as the combined result of heterogeneous Pb components that were co-deposited with the BIFs and variably opened U–Pb systems since their formation, most likely during the localized ~2.0 Ga tectono-metamorphic overprinting for which evidence is presented here. The latter explanation is best exemplified by sample MUPD 24-58D which yielded geologically unreasonably low *in situ* corrected $^{206}Pb/^{204}Pb$ and $^{207}Pb/^{204}Pb$ ratios that plot outside the limits of Fig. 15. Lead-loss is probably facilitated during U–Pb open-system behavior during metamorphic overprinting or metasomatic fluid percolation (e.g. Frei and Polat, 2007) and leads to significantly over-corrected initial Pb isotopic compositions as exemplified by this sample.

In situ corrected data points of BIF samples from Jim's Luck, Matsiloje and the Tau pit of the Mupane mine, however, define a relatively narrow data field which centers on the data point of the one galena sample from the Tau pit BIF. Since galena lead is insensitive to U–Pb open-system behavior it probably characterizes the initial Pb isotope signature in this BIF. Therefore, the composition of the galena is used to retrieve information regarding the extraction of this lead from an MORB-source as defined by Kramers and Tolstikhin (1997) (Pb growth curve plotted in Fig. 15). To explain the Pb isotopic signatures of the TGB BIFs, with respect to the ultimate Pb source, the following model is based on Fig. 15. A tangential line passing through the galena lead data point is fitted to the MORB

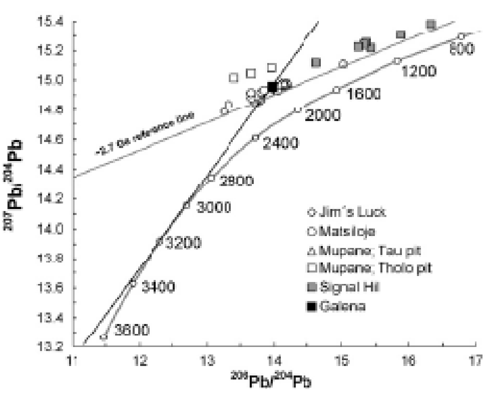

Fig. 15. Uranogenic common Pb isotope diagram with *in situ* (2.0 Ga) corrected data from the TGB BIFs and one galena from the Mupane mine. All data points plot to the left of the average MORB Pb source growth curve of Kramers and Tolstikhin (1997) (grey line). A tangential line passing through the galena fitted to this MORB curve yields an estimated mantle extraction age range of ~3.0–3.2 Ga. This age range is comparable to the Nd model ages (T_{DM}) of the BIF mesobands (see text for details).

source Pb growth curve of Kramers and Tolstikhin (1997) and this tangential line implies an estimated ~3.0–3.2 Ga model extraction age range of this Pb from an older Archean mantle reservoir. This age range overlaps well with the T_{DM} Nd model age range defined by the BIFs (3.16–3.27 Ga; Table 6) and is interpreted as the average extraction age of juvenile crustal portions with each their own U/Pb signatures which account for the observed spread particularly of $^{207}Pb/^{204}Pb$ ratios along the tangential line. The *in situ* Pb isotopic data arrays, which are parallel to ~2.7 Ga reference lines in Fig. 15, are interpreted as the result of resetting of the respective U–Pb isotope systems, possibly during a regional metamorphic event at around this time.

5.3. Inferences for sources of iron and silica

Hamade et al. (2003) in their study of BIFs from the Hamersley Range (Western Australia) showed that there is a hyperbolic trend of Ge/Si ratios versus SiO_2 for individual mesobands. These authors interpreted this relationship to indicate variable mixing of two compositionally different sources in BIF precipitation, one controlled by hydrothermal input (iron-rich) and the other by continentally derived input (silica-rich). The compatibility of Ge/Si versus SiO_2 hyperbolic trends in Hamersley BIFs and TGB BIFs (Fig. 10) suggests analogous processes. The overlap of the two curves in Fig. 10 also suggests a common mechanism for BIF precipitation in the Paleoproterozoic and Neoarchean eras, that is a two-source interaction model (e.g., Frei and Polat, 2007; Hamade et al., 2003). While Hamade et al. (2003) proposed hydrothermal (high Ge/Si, high Fe) and continental (low Ge/Si, high Si) inputs to explain variations in the Hamersley BIFs, Frei and Polat (2007), in a similar study conducted on the Isua (West Greenland) BIFs, added a further dimension to the discussion. Based on information obtained from Sm–Nd isotope data, these authors extended the two-source interaction model by introducing the likely association of REE- and Fe-sources. In doing so, Frei and Polat (2007) suggested that the high Ge/Si end of the series were associated with high Sm/Nd—elevated (positive) $\varepsilon_{Nd}(t)$ sources, typical of source regions that produce high-T, subaqueous hydrothermal fluids. In contrast, the low Ge/Si end of the series were defined by low Sm/Nd – lower (though still positive) $\varepsilon_{Nd}(t)$ values, compatible with derivation of Si from continental crust dominated by mafic rocks. One troubling aspect in the Ge/Si versus SiO_2 relationship is that there is no full understanding of the exact behavior of Ge during diagenesis of iron-rich sediments and whether the observed Ge/Si ratio in particularly silica-dominated mesobands is at all indicative of a weathered continental source (see discussion in Maliva et al., 2005). This is apparent when the TGB and Hamersley BIF curves are compared with data from the Isua (Western Greenland) BIFs (Frei and Polat, 2007; Fig. 10). The inferred hydrothermal Ge/Si end of the series in the Eoarchean Isua BIF is at least three times as high as that constrained by the TGB and Hamersley BIFs. In fact, the entire hyperbolic curve defined by the Isua BIF data is shifted towards higher Ge/Si values relative to the latter. This discrepancy was ascribed to varying source regions (Frei and Polat, 2007). However, a problem occurs because the inferred "pure" silica end of the series (ca. 79 wt % SiO_2) of the Isua BIF is also characterized by a roughly three times higher Ge/Si value relative to the value in the TGB and Hamersley BIFs (Fig. 10). Even if the stripping mechanism of Ge by precipitation of iron oxyhydroxides was the same for Eoarchean and Paleoproterozoic BIFs, the low Ge/Si end of the series should maintain the same magnitude. Whether or not the discrepancy lies solely in the increased and hotter Eoarchean hydrothermal input or in increased Ge removal on the weathering continents compared to the levels during Paleoproterozoic times remains unresolved and has to await further and more detailed studies.

Alexander et al. (2008) showed that for the ~2.9 Ga Pongola iron formation, high-*T* hydrothermal input of Nd in the contemporaneous sea water was less important and that most of the Nd in these seawater precipitates was derived from continental sources. Although this study did not report Fe concentrations on a mesoband scale for these BIFs to infer a REY correlation with potential Fe sources, these authors used Sm–Nd isotopes to identify REE solute sources in these chemical sediments. They based their interpretation on results showing that REY patterns of the Pongola BIFs are relatively depleted in HREE compared to the Eoarchean Isua (West Greenland) and the younger, Neoarchean Kuruman BIFs (South Africa), and they support their conclusions by presenting distinctly negative $\varepsilon_{Nd}(t)$ values (−1.9 to −4.3) for these BIFs. Modeling of hydrothermal versus continentally derived REE input fits the observed REE patterns and Nd isotopic data, which led these authors to suggest that mid- to late Archean shallow seawater was strongly influenced by continentally derived solute fluxes and challenged the conventional interpretation of using Sm–Nd isotopes versus Fe correlations to make inferences about the source of Fe in Archean seawater.

The correlations between Fe_2O_3 and Sm–Nd isotopes presented in Fig. 12A and B for the TGB BIFs contribute essentially to the understanding of the above outlined debate about the relative contributions of REE and Fe to the ambient seawater in general, and to the source characterization of components in the TGB BIFs in particular. The combined interpretation of these two figures implies that for the TGB BIFs the Fe-rich source is associated with a high Sm/Nd (extrapolated $^{147}Sm/^{144}Nd$ value of ~0.17) source and at the same time with a source that is significantly enriched ($\varepsilon_{Nd}(i) = -2.5$) relative to the Si-source ($\varepsilon_{Nd}(i) = -0.4$). Two explanations for these unusual relationships can be put forward: (1) the source reservoir for iron, instead of being the traditionally inferred hydrothermal high-*T* input, is the weathering hinterlands, i.e., continentally derived REE and Fe solutes. In contrast, the predominant high-end Si-rich mesobands in Fig. 10, would in this scenario be equated with high-*T* hydrothermal venting fluids. This would explain the link between the major BIF components Fe and Si and the respective Sm–Nd isotopic signatures. A similar conclusion, though not reached on the basis of identical lines of evidence, has been put forward by Alexander et al. (2008) for the ~2.9 Ga Pongola BIFs in South Africa. In their study, BIFs exhibit a range in $^{147}Sm/^{144}Nd$ that overlaps with the range defined by the TGB BIFs, with the highest values of ~0.17 coinciding with the inferred characteristics of the Fe-rich end-member defined in Fig. 12B. Based on the negative $\varepsilon_{Nd}(t)$ values measured for the Pongola BIFs these authors argued against mid-ocean ridge hydrothermal systems as the dominant REY sources but instead proposed that the solutes within shallow seawater along Archean cratonic margins were sources primarily from weathering of continental crust. If this scenario is accepted for the TGB BIFs, it would mean that Fe was derived essentially from the continents. Such a thought was also put forward by Alexander et al. (2008) in their study of the Pongola BIFs. However, an important point to emphasize is that, unlike the Pongola BIFs, where Alexander et al. (2008) present REY patterns with distinctly MREE-enriched humps explained by preferential adsorption of MREE on colloidal particles in many modern river's suspension loads (e.g., Elderfield et al., 1990), the TGB BIFs do not exhibit MREE-enrichments.

(2) Alternatively, if the Fe-rich reservoir is assumed to be related to high-T hydrothermal fluids and the negative $\varepsilon_{Nd}(t)$ characteristics of the source material, a possible scenario is that these fluids were derived from interaction with an enriched mantle source (explaining the negative $\varepsilon_{Nd}(t)$ values) and periodically mixed with shallow waters that obtained their signature through weathering of predominantly mafic crust on land (explaining the less negative $\varepsilon_{Nd}(t)$ values of the inferred Si-rich end-member). Isotopically, the low (negative) $\varepsilon_{Nd}(t)$ values defined by Fe-rich mesobands of

the TGB BIF are compatible with negative $\varepsilon_{Nd}(t)$ values (average of -1.3 ± 0.5; 1σ; Table 5) of volcanic rocks belonging to the Penhalonga Fm, which are directly associated with them, but not with basalts from the stratigraphically underlying Lady Mary Formation which are characterized by positive $\varepsilon_{Nd}(t)$ values (average of $+2.0 \pm 0.5$; excluding sample LM46; Table 6). In addition, the low Fe end-member with an inferred $\varepsilon_{Nd}(t)$ value of roughly -0.4 extrapolated from the Fe_2O_3/SiO_2 versus $\varepsilon_{Nd}(t)$ relationships of mesobands in BIF sample MAT-3C (Fig. 12B) compares well with the average $\varepsilon_{Nd}(t)$ value of -0.4 ± 1.1 defined by sedimentary rocks from within the TGB. This leads us to propose that surface basin waters were mixed with high-T fluid fertilized deeper waters which obtained their REE signature from weathering of continental crustal material similar in composition to the sedimentary rocks that are associated with the BIF in the TGB. Sm–Nd isotope data allow us to argue that these continental sources were significantly mafic in nature.

5.4. Inferences for the nature of the enriched mantle reservoir

Inferences from Sm–Nd isotope data indicate strongly negative initial ε_{Nd} values (high-T fluid end-member ε_{Nd} value of -2.5; see Fig. 12A and B) which indicate that the mantle sources from which these REE components were derived had experienced an earlier enrichment. Such enrichment, potentially by ancient recycling of continentally derived material into the mantle, is generally compatible with other lines of evidence. Thus, Re-Os isotopes of chromite-bearing layered intrusions in the Zimbabwe Craton (Nägler et al., 1997) as well as Re-Os and other isotope systematics of xenoliths from within kimberlites in the Kaapvaal Craton (Shirey et al., 2001; Shirey and Walker, 1998; Walker et al., 1989) support the existence of a long-lived ancient subcontinental lithospheric mantle beneath much of southern Africa. Recent studies, focusing on major-and trace-elemental characteristics as well as isotope geochemical (Lu-Hf, Sm–Nd, Pb) data on rift-related giant dyke swarms and associated lava flows and sills in southern Africa (for example, those of the Karoo province (Jourdan et al., 2007; Kobussen et al., 2008)) essentially confirmed the xenolith-based interpretations for the existence of a subcontinental lithospheric mantle and revealed that its extensions is far more widespread than initially assumed. Although there is some debate regarding the timing of the enrichment process, Os isotopic data on chromite and PGE alloys provided robust information for a long-lived and ancient Re depletion as far back as ∼3.8 Ga (Nägler et al., 1997). Griffin et al. (2003) provided a compositional and structural map in four dimensions of the lithospheric mantle underlying the Kaapvaal Craton and the surrounding mobile belts, and highlighted the strong vertical and lateral heterogeneity of this subcontinental lithospheric mantle. One of the most striking features is strong geochemical depletion in the depth interval 120–180 km below the Limpopo Belt. Jourdan et al. (2007) based on isotope geochemical signatures of high- and low-Ti basalts associated with the Karoo magmatic event, inferred that the distribution of these high- and low-Ti magmas reflects strong control by lithospheric architecture. They emphasized that high-Ti magmas are restricted to the thick Limpopo Belt lithosphere, whereas the low-Ti magmas are located on the thinner Kaapvaal and Zimbabwe cratonic lithospheres. These authors explained the low-$\varepsilon_{Nd(i)}$, low-$\varepsilon_{Hf(i)}$, and low-$^{206}Pb/^{204}Pb_i$ signatures of these basalts by postulating a mantle source that was previously enriched to high degrees by subduction related metasomatism (and sediment input?) beneath the Limpopo Belt. In the light of these results, the REE and Sm–Nd isotopic signatures of the TGB BIF and associated volcanic rocks are preferably tied to sources derived from subcontinental lithospheric mantle or similar enriched reservoirs that existed ∼2.7 Ga ago beneath cratonic regions eastern Botswana.

6. Conclusions

The main objective of this study was to delineate the source of components in TGB BIFs by means of (isotope-) geochemical data and the following conclusions can be drawn:

REY data sets for individual mesobands from the TGB BIFs show characteristic features resembling those of other Archean BIFs worldwide (with PAAS normalized LREE and MREE depleted REY patterns relative to HREE, positive La/La^*_{PASS}, Eu/Eu^*_{PASS}, Y/Ho and no Ce/Ce^*_{PASS} anomalies). With the exception of Eu and Ce anomalies, these are characteristic features of modern seawater.

Elevated Eu/Eu^*_{PASS} anomalies relative to the Paleoproterozoic Hamersley (Western Australia) BIF in TGB BIFs are symptomatic of worldwide BIFs deposited at around 2.6–2.7 Ga and indicate a period when high mantle heat flow allowed increased hydrothermal pulses to be injected into contemporaneous seawater.

Uranogenic Pb isotope data for the BIFs define separate correlation trajectories with slopes corresponding to ∼2.7 Ga. These trend lines lie at elevated $^{207}Pb/^{204}Pb$ relative to $^{206}Pb/^{204}Pb$ values and imply a high-μ prehistory of their source materials. The initial leads in the BIFs can best be explained by ∼3.0–3.2 Ga extraction of Pb from an older Archean mantle reservoir, subsequent evolution of individual source reservoirs with variable U/Pb ratios and incorporation of these signatures into the chemical sediments at ∼2.7 Ga, and finally by a resetting of the whole-rock U–Pb systems during a regional metamorphic event shortly following thereafter.

Local tectono-metamorphic overprinting, exemplified by the Mupane BIFs and by PbSL data of garnets from associated sedimentary rocks, occurred at 1976 ± 88 Ma. This overprinting is interpreted as being related to the ∼2.0 Ga tectono-metamorphic event characteristic of the adjacent Limpopo Mobile Belt. How far the effects of the Limpopo deformational events can be traced into the Zimbabwe Craton cannot be judged from this study. Additional Pb isotopic analyses on single minerals from other greenstone belts are required to clarify this. The fact that the 2.0 Ga Limpopo metamorphism seems to have affected the southern cratonic areas, as exemplified by our results on the Mupane BIF, might be of importance for future gold exploration programs in other greenstone belts within the southern Zimbabwe Craton.

Ge/Si ratios also point to source decoupling of Si and Fe in respective BIF mesobands. The hyperbolic relationship between Ge/Si ratios and Fe_2O_3 matches that defined by other BIFs, particular the ∼2.45 Ga Hamersley BIFs (Western Australia), and calls for independent sources for Fe and Si similar to those inferred from the Sm/Nd–Fe_2O_3 relationship.

The average depleted mantle Nd model age defined by BIF mesobands is 3.22 ± 0.21 Ga, compatible with the extraction period inferred from Pb isotopes. While the five BIFs from the TGB cannot be distinguished by their Sm–Nd isotopic compositions, the subtle differences in their Pb isotopic signatures imply small but distinct differences in surface water compositions or in the source of detrital components that were incorporated during the deposition of these chemical sedimentary rocks.

Sm–Nd isotopic relationships between Si- and Fe-rich mesobands of one of the TGB BIFs studied in detail allow for a more precise characterization of these sources. The first one is exemplified by elevated Sm/Nd ratios, negative ε_{Nd} values (inferred end-member $\varepsilon_{Nd} = -2.5$) and is associated with high Fe-fluxes. The second one is characterized by relatively low Sm/Nd ratios, less negative ε_{Nd} values (inferred end-member $\varepsilon_{Nd} = -0.4$) and is associated with high Si fluxes. These sources represent, respectively (1) seafloor-vented hydrothermal fluids that received their Sm–Nd isotopic signature from enriched oceanic crustal rocks, and (2) ambient surface basin waters whose REE signature was controlled by solutes derived from weathering of nearby continental landmasses with a likely average mafic composition.

The negative ε_{Nd} signature of the high-T fluid source may point to the existence of subcontinental lithospheric mantle components beneath the Kaapvaal and Zimbabwe cratons, for which independent evidence exists from the study of layered intrusions, kimberlite hosted xenoliths and rift related volcanic rocks.

Acknowledgments

Thanks to the mining company IAMGold (former Gallery Gold) for providing drill cores, access to the area in and around the Mupane mine and for logistical support.

In addition, we thank the following people for their contributions to results presented in this manuscript: Toby Leeper for helping with TIMS analyses, Maria Jankowski and Toni Larsen for assisting with chemical separation procedures; Jørgen Kystol for analyzing the ICP-MS samples; Hanne Lamberts for preparing thin sections; Peter Venslev for assisting with mineral separation; and John Bailey for performing the XRF analyses and useful informal review. We thank Kurt Konhauser for providing the original Ge/Si ratio data set for the Hamersley BIF. Finally, we thank the two reviewers Andrey Bekker and Ali Polat for valuable comments on our manuscript.

This study was funded by the Danish Research Agency FNU (Forskningsrådet for Natur og Univers) grant no. 21-01-0492 to Robert Frei.

References

Alexander, B.W., Bau, M., Andersson, P., Dulski, P., 2008. Continentally-derived solutes in shallow Archean seawater: Rare earth element and Nd isotope evidence in iron formation from the 2.9 Ga Pongola Supergroup, South Africa. Geochimica et Cosmochimica Acta 72 (2), 378–394.

Alibert, C., McCulloch, M.T., 1993. Rare-earth element and neodymium isotopic compositions of the banded iron-formations and associated shales from Hamersley, Western Australia. Geochimica et Cosmochimica Acta 57 (1), 187–204.

Alibo, D.S., Nozaki, Y., 1999. Rare earth elements in seawater: particle association, shale-normalization, and Ce oxidation. Geochimica et Cosmochimica Acta 63 (3–4), 363–372.

Anders, E., Grevesse, N., 1989. Abundances of the elements—meteoritic and solar. Geochimica et Cosmochimica Acta 53 (1), 197–214.

Bagai, Z., Armstrong, R., Kampunzu, A.B., 2002. U–Pb single zircon geochronology of granitoids in the Vumba granite-greenstone terrain (NE Botswana): implications for the evolution of the Archaean Zimbabwe craton. Precambrian Research 118 (3–4), 149–168.

Bau, M., 1993. Effects of syn-depositional and postdepositional processes on the rare-earth element distribution in Precambrian iron-formations. European Journal of Mineralogy 5 (2), 257–267.

Bau, M., 1996. Controls on the fractionation of isovalent trace elements in magmatic and aqueous systems: evidence from Y/Ho, Zr/Hf, and lanthanide tetrad effect. Contributions to Mineralogy and Petrology 123 (3), 323–333.

Bau, M., 1999. Scavenging of dissolved yttrium and rare earths by precipitating iron oxyhydroxide: experimental evidence for Ce oxidation, Y-Ho fractionation, and lanthanide tetrad effect. Geochimica et Cosmochimica Acta 63 (1), 67–77.

Bau, M., Dulski, P., 1992. Small-scale variations of the rare-earth element distribution in Precambrian iron-formations. European Journal of Mineralogy 4 (6), 1429–1433.

Bau, M., Möller, P., 1993. Rare-earth element systematics of the chemically precipitated component in early Precambrian iron formations and the evolution of the terrestrial atmosphere-hydrosphere-lithosphere system. Geochimica et Cosmochimica Acta 57 (10), 2239–2249.

Bau, M., Dulski, P., 1996. Distribution of yttrium and rare-earth elements in the Penge and Kuruman iron-formations, Transvaal Supergroup, South Africa. Precambrian Research 79 (1–2), 37–55.

Bau, M., Dulski, P., 1999. Comparing yttrium and rare earths in hydrothermal fluids from the Mid-Atlantic Ridge: implications for Y and REE behaviour during near-vent mixing and for the Y/Ho ratio of Proterozoic seawater. Chemical Geology 155 (1–2), 77–90.

Berger, M., Rollinson, H., 1997. Isotopic and geochemical evidence for crust-mantle interaction during late Archaean crustal growth. Geochimica et Cosmochimica Acta 61 (22), 4809–4829.

Beukes, N., 2004. Biogeochemistry—Early options in photosynthesis. Nature 431 (7008), 522–523.

Bickle, M.J., Nisbet, E.G., Martin, A., 1994. Archean greenstone belts are not oceanic-crust. Journal of Geology 102 (2), 121–138.

Blenkinsop, T.G., Martin, A., Jelsma, H.A., Vinyu, M.L., 1997. The Zimbabwe Craton. In: de Wit, M.J., Ashwal, L.D. (Eds.), Tectonic evolution of Greenstone Belts. Oxford University Monograph on Geology and Geophysics, pp. 567–580.

Bolhar, R., Kamber, B.S., Moorbath, S., Fedo, C.M., Whitehouse, M.J., 2004. Characterisation of early Archaean chemical sediments by trace element signatures. Earth and Planet. Sci. Lett. 222 (1), 43–60.

Boshoff, R., Van Reenen, D.D., Smit, C.A., Perchuk, L.L., Kramers, J.D., Armstrong, R., 2006. Geologic history of the Central Zone of the Limpopo Complex: The West Alldays area. Journal of Geology 114 (6), 699–716.

Chown, E.H., N'Dah, E., Mueller, W.U., 2000. The relation between iron-formation and low temperature hydrothermal alteration in an Archean volcanic environment. Precambrian Research 101 (2–4), 263–275.

Condie, K.C., 1997. Plate Tectonics and Crustal Evolution. Butterworth-Heinemann, Oxford, 282 pp.

Condie, K.C., 1998. Episodic continental growth and supercontinents: a mantle avalanche connection? Earth and Planetary Science Letters 163 (1–4), 97–108.

Coward, M.P., 1976. Archaean deformation patterns in Southern-Africa. Philosophical Transactions of the Royal Society of London Series A: Mathematical Physical and Engineering Sciences 283 (1312), 313–331.

Danielson, A., Möller, P., Dulski, P., 1992. The europium anomalies in banded iron formations and the thermal history of the oceanic crust. Chemical Geology 97 (1–2), 89–100.

DePaolo, D.J., 1981. Neodymium isotopes in the Colorado Front Range and crust-mantle evolution in the Proterozoic. Nature 291 (5812), 193–196.

Derry, L.A., Jacobsen, S.B., 1990. The chemical evolution of Precambrian seawater - Evidence from REEs in banded iron formations. Geochimica et Cosmochimica Acta 54 (11), 2965–2977.

Dirks, P., Jelsma, H.A., 1998. Horizontal accretion and stabilization of the Archean Zimbabwe craton. Geology 26 (1), 11–14.

Dodson, M.H., Williams, I.S., Kramers, J.D., 2001. The Mushandike granite: further evidence for 3.4 Ga magmatism in the Zimbabwe craton. Geological Magazine 138 (1), 31–38.

Elderfield, H., Upstillgoddard, R., Sholkovitz, E.R., 1990. The rare earth elements in rivers, estuaries, and coastal seas and their significance to the composition of ocean waters. Geochimica et Cosmochimica Acta 54 (4), 971–991.

Fedo, C.M., Eriksson, K.A., 1996. Stratigraphic framework of the similar to 3.0 Ga Buhwa greenstone belt: a unique stable-shelf succession in the Zimbabwe Archean Craton. Precambrian Research 77 (3–4), 161–178.

Frei, R., Kamber, B.S., 1995. Single Mineral Pb–Pb dating. Earth and Planetary Science Letters 129 (1–4), 261–268.

Frei, R., Polat, A., 2007. Source heterogeneity for the major components of ~3.7 Ga banded iron formations (Isua Greenstone Belt, Western Greenland): Tracing the nature of interacting water masses in BIF formation. Earth and Planetary Science Letters 253 (1–2), 266–281.

Frei, R., Bridgwater, D., Rosing, T., Stecher, O., 1999. Controversial Pb-Pb and Sm-Nd isotope results in the early Archean Isua (West Greenland) oxide iron formation: Preservation of primary signatures versus secondary disturbances. Geochimica et Cosmochimica Acta 63 (3–4), 473–488.

Frei, R., Dahl, P.S., Duke, E.F., Frei, K.M., Hansen, T.R., Frandsson, M.M., Jensen, L.A., 2008. Trace element and isotopic characterization of Neoarchean and Paleoproterozoic iron formations in the Black Hills (South Dakota, USA): Assessment of chemical change during 2.9–1.9 Ga deposition bracketing the 2.4–2.2 Ga first rise of atmospheric oxygen. Precambrian Research 162 (3–4), 441–474.

Fryer, B.J., 1977. Rare earth evidence in iron-formations for changing Precambrian oxidation states. Geochimica et Cosmochimica Acta 41 (3), 361–367.

German. C.R., Von Damm. K.L. 2007. Hydrothermal processes. In: Holland. H.D., Turekain, K.K. (Eds.), Treatise on Geochemistry. Elsevier Ltd, pp. 181–222.

Griffin, W.L., O'Reilly, S.Y., Natapov, L.M., Ryan, C.G., 2003. The evolution of lithospheric mantle beneath the Kalahari Craton and its margins. Lithos 71 (2–4), 215–241.

Hamade, T., Konhauser, K.O., Raiswell, R., Goldsmith, S., Morris, R.C., 2003. Using Ge/Si ratios to decouple iron and silica fluxes in Precambrian banded iron formations. Geology 31 (1), 35–38.

Holzer, L., Frei, R., Barton, J.M., Kramers, J.D., 1998. Unraveling the record of successive high grade events in the Central Zone of the Limpopo Belt using Pb single phase dating of metamorphic minerals. Precambrian Research 87 (1–2), 87–115.

Hunter, M.A., Bickle, M.J., Nisbet, E.G., Martin, A., Chapman, H.J., 1998. Continental extensional setting for the Archean Belingwe Greenstone Belt, Zimbabwe. Geology 26 (10), 883–886.

Jourdan, F., Bertrand, H., Scharer, U., Blichert-Toft, J., Feraud, G., Kampunzu, A.B., 2007. Major and trace element and Sr, Nd, Hf and Pb isotope compositions of the Karoo large igneous province, Botswana-Zimbabwe: Lithosphere vs mantle plume contribution. Journal of Petrology 48 (6), 1043–1077.

Kalsbeek, F., Frei, R., 2006. The Mesoproterozoic Midsommerso dolerites and associated high-silica intrusions, North Greenland: crustal melting, contamination and hydrothermal alteration. Contributions to Mineralogy and Petrology 152 (1), 89–110.

Kamber, B.S., Blenkinsop, T.G., Villa, I.M., Dahl, P.S., 1995. Proterozoic transpressive deformation in the Northern Marginal Zone, Limpopo Belt, Zimbabwe. Journal of Geology 103 (5), 493–508.

Kampunzu, A.B., Tombale, A.R., Zhai, M., Bagai, Z., Majaule, T., Modisi, M.P., 2003. Major and trace element geochemistry of plutonic rocks from Francistown, NE Botswana: evidence for a Neoarchaean continental active margin in the Zimbabwe craton. Lithos 71 (2–4), 431–460.

Kappler, A., Pasquero, C., Konhauser, K.O., Newman, D.K., 2005. Deposition of banded iron formations by anoxygenic phototrophic Fe(II)-oxidizing bacteria. Geology 33 (11), 865–868.

Kato, Y., Yamaguchi, K.E., Ohmoto, H., 2006. Rare earth elements in Precambrian banded iron formations: Secular changes of Ce and Eu anomalies and evolution of atmospheric oxygen. In: Kesler, S.E., Ohmoto, H. (Eds.), Evolution of Early Earth's Atmosphere, Hydrosphere, and Biosphere. Geological Society of America, pp. 269–289.

Key, R., 1976. The geology of the area around Francistown and Phikwe, Northeast and Central Districts, Botswana. District Memoir 3. Geological Survey of Botswana, 121 pp.

Key, R.M., Litherland, M., Hepworth, J.V., 1976. The evolution of the Archaean crust of northeast Botswana. Precambrian Research 3 (4), 375–413.

Klein, C., Beukes, N.J., 1989. Geochemistry and sedimentology of a facies transition from limestone to iron-formation deposition in the early Proterozoic Transvaal Supergroup, South Africa. Economic Geology 84 (7), 1733–1774.

Kobussen, A.F., Griffin, W.L., O'Reilly, S.Y., Shee, S.R., 2008. Ghosts of lithospheres past: Imaging an evolving lithospheric mantle in southern Africa. Geology 36 (7), 515–518.

Konhauser, K.O., Hamade, T., Raiswell, R., Morris, R.C., Ferris, F.G., Southam, G., Canfield, D.E., 2002. Could bacteria have formed the Precambrian banded iron formations? Geology 30 (12), 1079–1082.

Kramers, J.D., Tolstikhin, I.N., 1997. Two terrestrial lead isotope paradoxes, forward transport modelling, core formation and the history of the continental crust. Chemical Geology 139 (1–4), 75–110.

Kreissig, K., Nagler, T.F., Kramers, J.D., van Reenen, D.D., Smit, C.A., 2000. An isotopic and geochemical study of the northern Kaapvaal Craton and the Southern Marginal Zone of the Limpopo Belt: are they juxtaposed terranes? Lithos 50 (1–3), 1–25.

Kreissig, K., Holzer, L., Frei, R., Villa, I.M., Kramers, J.D., Kroner, A., Smit, C.A., van Reenen, D.D., 2001. Geochronology of the Hout River Shear Zone and the metamorphism in the southern marginal zone of the Limpopo Belt, Southern Africa. Precambrian Research 109 (1–2), 145–173.

Kusky, T.M., 1998. Tectonic setting and terrane accretion of the Archean Zimbabwe craton. Geology 26 (2), 163–166.

Kusky, T.M., Kidd, W.S.F., 1992. Remnants of an Archean oceanic plateau, Belingwe Greenstone-Belt, Zimbabwe. Geology 20 (1), 43–46.

Ludwig, K.R., 2003. User's Manual for Isoplot 3.00: a Geochronological Toolkit for Microsoft Excel. Berkely Geochronology Center, 70 pp.

Majaule, T., Davis, D.W., 1998. U–Pb zircon dating and geochemistry of granitoids in the Mosetse area, NE Botswana, and tectonic implications. In: Geological Survey of Botswana, 30th Anniversary International Conference Abstract volume, pp. 46–48.

Maliva, R.G., Knoll, A.H., Simonson, B.M., 2005. Secular change in the Precambrian silica cycle: Insights from chert petrology. Geological Society of America Bulletin 117 (7–8), 835–845.

McCourt, S., Kampunzu, A.B., Bagai, Z., Armstrong, R.A. 2004. The crustal architecture of Archaean terranes in northeastern Botswana. South African Journal of Geology 107 (1–2), 147–158.

Morris, R.C., 1993. Genetic modeling for banded iron-formation of the Hamersley Group, Pilbara Craton, Western Australia. Precambrian Research 60 (1–4), 243–286.

Mueller, W.U., Mortensen, J.K., 2002. Age constraints and characteristics of subaqueous volcanic construction, the Archean Hunter Mine Group, Abitibi greenstone belt. Precambrian Research 115 (1–4), 119–152.

Nozaki, Y., Zhang, J., Amakawa, H., 1997. The fractionation between Y and Ho in the marine environment. Earth and Planetary Science Letters 148 (1–2), 329–340.

Nägler, T.F., Kramers, J.D., Kamber, B.S., Frei, R., Prendergast, M.D.A., 1997. Growth of subcontinental lithospheric mantle beneath Zimbabwe started at or before 3.8 Ga: Re-Os study on chromites. Geology 25 (11), 983–986.

Posth, N.R., Hegler, F., Konhauser K.O., Kappler, A., 2008. Alternating Si and Fe deposition caused by temperature fluctuations in Precambrian oceans. Nature Geoscience 1 (10), 703–708.

Roering, C., Vanreenen, D.D., Smit, C.A., Barton, J.M., Debeer, J.H. Dewit, M.J., Stettler, E.H, Vanschalkwyk, J.F., Stevens, G., Pretorius, S., 1992. Tectonic model for the evolution of the Limpopo Belt. Precambrian Research 55 (1–4), 539–552.

Rudnick, R.L., Gao, S., 2004. Composition of the continental crust. In: Holland, H.D., Turekain, K.K. (Eds.), Treatise on Geochemistry. Elsevier, pp. 1–64.

Schaller, M., Steiner, O., Studer, I., Frei, R., Kramers, J.D., 1997. Pb stepwise leaching (PbSL) dating of garnet-addressing the inclusion problem. Schweizerische Mineralogische und Petrographische Mitteilungen 77 (1), 113–121.

Shimizu, K., Nakamura, E., Maruyama, S., 2005. The geochemistry of ultramafic to mafic volcanics from the Belingwe greenstone belt, Zimbabwe: Magmatism in an Archean continental large igneous province. Journal of Petrology 46 (11), 2367–2394.

Shirey, S.B., Walker, R.J., 1998. The Re-Os isotope system in cosmochemistry and high-temperature geochemistry. Annual Review of Earth and Planetary Sciences 26, 423–500.

Shirey, S.B., Carlson, R.W., Richardson, S.H., Menzies, A., Gurney, J.J., Pearson, D.G., Harris, J.W., Wiechert, U., 2001. Archean emplacement of eclogitic components into the lithospheric mantle during formation of the Kaapvaal Craton. Geophysical Research Letters 28 (13), 2509–2512.

Slack, J.F., Grenne, T., Bekker, A., Rouxel, O.J., Lindberg, P.A., 2007. Suboxic deep seawater in the late Paleoproterozoic: Evidence from hematitic chert and iron formation related to seafloor-hydrothermal sulfide deposits, central Arizona, USA. Earth and Planetary Science Letters 255 (1–2), 243–256.

Stacey, J.S., Kramers, J.D., 1975. Approximation of terrestrial lead isotope evolution by a 2-stage model. Earth and Planetary Science Letters 26 (2), 207–221.

Stein, M., Hofmann, A.W., 1994. Mantle plumes and episodic crustal growth. Nature 372 (6501), 63–68.

Taylor, S.R., McLennan, S.M., 1985. The Continental Crust: It's Composition and Evolution. Blackwell, Oxford, 312 pp.

Todt, W., Cliff, R.A., Hanser, A., Hofmann, A.W., 1993. Re-calibration of NBS lead standards using $^{202}Pb + ^{205}Pb$ double spike. Terra Abstract 5, 396.

Walker, R.J., Carlson, R.W., Shirey, S.B., Boyd, F.R., 1989. Os, Sr, Nd, and Pb isotope systematics of southern African peridotite xenoliths: Implications for the chemical evolution of subcontinental mantle. Geochimica et Cosmochimica Acta 53 (7), 1583–1595.

Webb, G.E., Kamber, B.S., 2000. Rare earth elements in Holocene reefal microbialites: A new shallow seawater proxy. Geochimica et Cosmochimica Acta 64 (9), 1557–1565.

Wilson, J.F., Nesbitt, R.W., Fanning, C.M., 1995. Zircon geochronology of Archaean felsic sequences in the Zimbabwe craton: a revision of greenstone stratigraphy and a model for crustal growth. In: Coward, M.P., Ries, A.C. (Eds.), Early Precambrian Processes, vol. 95. Geological Society London, pp. 109–126 (Special Publications).

Zeh, A., Gerdes, A., Klemd, R., Barton, J.M., 2007. Archaean to Proterozoic crustal evolution in the Central Zone of the Limpopo Belt (South Africa-Botswana): Constraints from combined U–Pb and Lu–Hf isotope analyses of zircon. Journal of Petrology 48 (8), 1605–1639.

Zhai, M., Kampunzu, A.B., Modisi, M.P., Bagai, Z., 2006. Sr and Nd isotope systematics of Francistown plutonic rocks, Botswana: implications for Neoarchaean crustal evolution of the Zimbabwe craton. International Journal of Earth Sciences 95 (3), 355–369.